EUROPEAN JOURNAL OF PURE AND APPLIED MATHEMATICS
2025, Vol. 18, Issue 4, Article Number 6395
ISSN 1307-5543 – ejpam.com
Published by New York Business Global

Squeeze Flow of Ethylene Glycol-based Carbon Nanotube with the Influence of Joule Heating, Viscous Dissipation and Chemical Reactions

Naseer Khan[1], Muhammad Farooq[1], Wajid Ullah Jan[1], Berna Uzun[2,3], Dragan Pamucar[4,*], Ilker Ozsahin[2], Hijaz Ahmad[2,5,6,*]

[1] *Department of Mathematics, Abdul Wali Khan University Mardan, KP, Pakistan*
[2] *Operational Research Center in Healthcare, Near East University, Nicosia/TRNC, 99138 Mersin 10, Turkey*
[3] *Department of Mathematical Sciences, Saveetha School of Engineering, SIMATS, Chennai, Tamilnadu, India*
[4] *Széchenyi István University, Gyor, Hungary*
[5] *VSB–Technical University of Ostrava, CEET, ENET Centre, 17. listopadu 2172/15, 708 00 Ostrava–Poruba, Czech Republic*
[6] *Department of Mathematics, College of Science, Korea University, 145 Anam-ro, Seongbuk-gu, Seoul 02841, Republic of Korea*

Abstract. In this article, we discuss a hydrothermal model that describes the flow of Carbon Nanotube nanofluid between squeezing plates while accounting for joule heating, viscous dissipation and homogeneous-heterogeneous chemical reactions. The (*Alumina*) and Carbon Nanotubes (single-wall carbon nanotube or multi-wall carbon nanotube) have been used as nanoparticles with a base fluid Ethylene glycol with water ($Alumina + C_2H_6O_2 - H_2O$). The homotopy analysis technique included into Mathematica and the MATLAB worked in BVP4c are used to approve and verify the results. We obtain that excellent agreement is observed between the semi-analytical Homotopy analysis method solutions and the numerical bvp4c results, demonstrating the high accuracy and reliability of the adopted methodologies. The residual errors of the Homotopy analysis method have been shown physically and numerically for single-wall carbon nanotube and multi-wall carbon nanotube. The other embedding parameters like Reynolds squeeze parameter S_r, Prandtl number P_r^*, volume fraction ϕ_1, ϕ_2, schmit number S_r^* and Eckert numbers E_1, E_2 have been intended and discussed. The aim of this research is the improvement towards the consumption of energy in the field of engineering and industry. Furthermore, from the results it has been noted that the based on the data the multi-wall carbon nanotubes have a stronger effect on velocity, temperature distribution, homogeneous and heterogeneous chemical reactions profiles, which is shown by graphs and tables.

2020 Mathematics Subject Classifications: 76A02, 76D05, 76M55, 76V05, 80M40

*Corresponding author.
*Corresponding author.
DOI: https://doi.org/10.29020/nybg.ejpam.v18i4.6395

Email addresses: pamucar.dragan@sze.hu (D. Pamucar), hijaz.ahmad@neu.edu.tr (H. Ahmad)

Key Words and Phrases: Squeezing plates, nanofluid, homogeneous and heterogeneous chemical reaction

1. Introduction

Industry and engineering require materials to cool quickly and to transfer heat quickly, both of which consume time and energy. The majority of researchers have employed nanofluid in the last ten years for improving cooling and heat transfer rates. Nanofluid is created when liquids and tiny particles (between 1 and 100 nm in size) are combined. These particles are often utilized in the nanofluid solution up to a 5 percent concentration. One significant family of carbon in both single- and multiple-walled forms is carbon nanotubes. The term "ponder nanomaterial" is commonly used to describe carbon nanotubes, which have a large angle proportion and a very broad range of unique mechanical, chemical, thermal, and optical characteristics. Because of their unique qualities, carbon nanotubes are one of the most popular exchange materials in the materials sciences. Iijimain [1], Endo, and associates [2] deserve recognition for their pioneering work on the in-depth analysis of TEM images of the carbon nanotube in 1976. They demonstrated the arrangement of carbon tubes that were nanoscale (with lengths ranging from 4 to 30 nm) and tube-like using the circular segment release vanishing approach. The researchers devised the process for adopting the single wall carbon nanotubes later in 1993 [3, 4]. Since their gradual discovery in the early 1990s, carbon nanotubes have sparked a frenzied interest among academics and modernists alike due to their fascinating characteristics and latent uses in various industries, including aviation, electronics, automotive, optical, and vitality transformation [5, 6]. The heat transfer enhancement in shell and tube heat exchangers using a tri-hybrid nanofluid suspension consisting of copper (Cu), iron oxide (Fe_3O_4), and multiwall carbon nanotubes dispersed in water as the base fluid by F. Mebarek-Oudina [7]. The thermal transport and entropy generation in viscous flow over a radially stretching disk, incorporating the effects of magnetohydrodynamics (MHD), viscous dissipation, Joule heating, and radiation was study by Tahir Naseem [8]. The influence of geometric parameters on free convective heat transfer in a zigzag-walled cavity filled with a hybrid nano-fluid composed of magnesium oxide (MgO) and single-walled carbon nanotubes suspended in water was studied by F. Mebarek-Oudina [9]. Many researchers used various experimental methodologies in an attempt to increase the carbon nanotubes thermal efficiency. Qiu et al. [9] have investigated a unique quantitative comparison between the heat transfer contributions from thermal contact resistance at the carbon nanotubes array-solid interface (RC) and those from the thermal conductivity of the carbon nanotubes array (kCNT). carbon nanotubes-based electrical and thermal control in nanodevices is incredibly powerful. To create practical strategies for lowering the resistance at the bundle-bundle contact, Qiu et al. [10] used an experimental method. Recent reviews and summaries of Chinese research breakthroughs in the area of nanoscale heat transport characteristics have been provided by Qiu et al. [11]. They examined developments in atomic-level simulations as well as experimental advancements for certain types of nanoscale materials and architectures. Us-

ing the convective physical state, Zaidi et al. [12] investigated the wall jet streaming of carbon nanotubes nanofluid. Using an optimum and numerical technique, they examined the effects of the embedded factors. The single-walled carbon nanotubes and multi-walled carbon nanotubes over an upright cone under convective physical circumstances have been examined by Sreedevi et al. [13]. Haq et al. [14] used engine oil as the basis fluid in their investigation of carbon nanotubes. They looked at the nanofluid that was flowing between the concentric tubes. Sheikholeslami and Seyednezhad [15] used a water-based nanofluid to study the rapid heat transfer caused by the nonlinear magnetic field. Mechanical engineering relies heavily on thin-layer diffusion, which has important applications for coating processes. To connect the liquid's diffusion with various types of sheets, discs, wires, fibers, etc., these coating applications require comprehensive knowledge. Refs. [16, 17] provide the seminal work regarding the fundamental idea and mathematical modeling associated with thin layer streaming. The majority of studies first employed the thin layer's constant thickness. However, when nanofluid was developed, researchers [18–22] presented the idea of variable thickness for a bit better heat transmission and cooling process. Rehman et al.'s study [23] used kerosene, engine oil, and water as base fluids to investigate how to improve the thermal conductivities of carbon nanotubes. Ellahi et al.'s [24] study of nanofluid flow used a combination of carbon nanotubes and salt water. The rubber and plastic industries employ varieties of extending sheets for everyday applications. These sheets are shaped like tubes, plates, ellipses, circles, cones, and spheres. The radially extended surfaces have several uses in bioengineering and are connected to bilateral symmetry, rubber tires, and the radial artery. A radial disc's fluid flow along its expanding surface has been studied by Sajjad et al. [25]. The thin layer streaming across a nonlinear expanding surface has been studied by Gul [26]. We were sufficiently inspired to investigate this subject after reading about the aforementioned evaluation, in which many researchers examined distinct logical liquids together with various nanoparticles and produced significant warmth credits. Above all, they focused only on the attractive and slight impacts on cross-breed nanofluid while analyzing the aluminum composites of AA7072 and AA7072 + AA7075 in methanol fluid. According to the Lorentz forces found in this study, a hybrid nanofluid is less effective than a nanofluid. According to the literature, no study has yet thoroughly investigated the combined consequences of unstable flow between two squeezing plates when carbon nanotube nanoparticles are present. Consequently, we examined the impacts of a diverse and uniform chemical reaction on the flow between two squeezing plates in the presence of carbon nanotubes nanoparticles, utilizing all of the data. The combined inclusion of Joule heating, viscous dissipation, and homogeneous–heterogeneous chemical reactions offers new insight into their interplay on heat and mass transfer behavior. We conducted a systematic exploration of squeeze flow using hybrid nanofluids (carbon nanotubes + alumina nanoparticles), an area that has not been comprehensively addressed in prior studies. The Navier–Stokes equations, incorporating Joule heating, viscous dissipation, and homogeneous–heterogeneous processes, are solved using MATLAB (BVP4c) and the homotopy analysis method implemented in Mathematica.

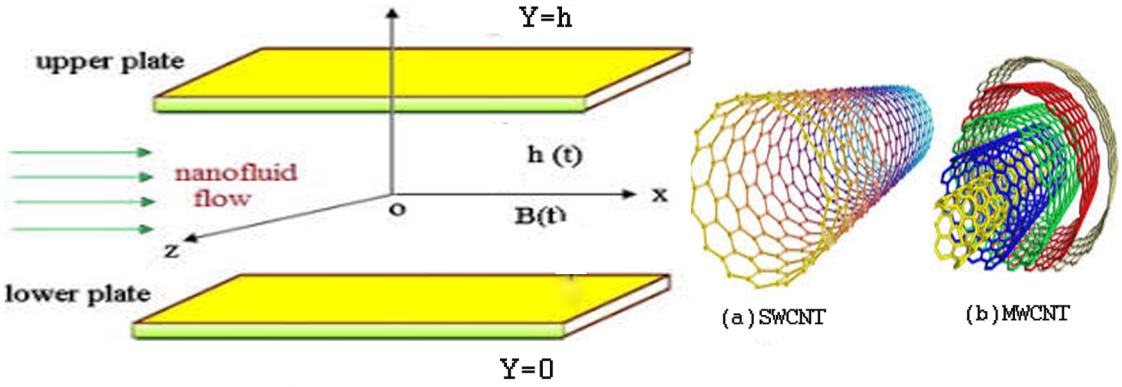

Figure 1: Problem Geometry

2. Mathematical Formulation

We take a laminar, incompressible, and carbon nanotubes-based nanofluid flow between horizontally parallel and squeezing plates with homogeneous and heterogeneous chemical reactions; Joule heating and viscous dissipation are seen in Figure 1. Ethylene glycol with water is taken as the base fluid. The carbon nanotubes are used as nanoparticles in the base fluids. The distance between the plates is $h(t) = l\sqrt{1-\alpha t}$, where α is the characteristic parameter of the squeezing motion and l represents the initial distance of the plate at t = 0. The plates are separated while $\alpha < 0$, but when $\alpha > 0$, they compress until they meet at $t = \frac{1}{\alpha}$. A homogenous magnetic field spread in the y-axis, $B^*(t) = \frac{B_0^*}{\sqrt{1-\alpha t}}$, frequently affects the velocity field. The temperature of both top and lower plates remains constant, i.e., ξ_i and ξ_j recursively. An investigation of Joule heating and viscous dissipation is made in the presence of a carbon nanotubes nanofluid. For cubic autocatalysis, the homogeneous reaction is as follows:

$$\Omega 1 + 2\Omega 2 \rightarrow 3\Omega 2, \tag{1}$$

and the concentration rate is $K_c a^*(b^*)^2$, where as heterogeneous reaction on the catalyst surface, is

$$\Omega 1 \rightarrow \Omega 2, \tag{2}$$

a^* and b^* respectively, represent the concentration of the chemical species Ω_1 and Ω_2, while k_c^* represents the rate constants. As the following equations illustrate, an external flow, the reaction rate vanishes beyond the boundary layer edge. Mass, momentum, thermal energy, homogeneous, and heterogeneous reaction conservation that is time-dependent may be determined in the Cartesian coordinates (x, y) obtained at the bottom plate center [27–30]. Here we use for equation and tables the abbreviation like (CNT for carbon nan-

otube, single wall carbon nanotube (SWCNT), multi wall carbon nanotube (MWCNT), Homotopy analysis method(HAM)).

Mass of conservation equation is expressed as,

$$\frac{\partial \psi}{\partial x} + \frac{\partial \upsilon}{\partial y} = 0. \tag{3}$$

Conservation equation of momentum as,

$$\frac{\partial \psi}{\partial t} + \psi \frac{\partial \psi}{\partial x} + \upsilon \frac{\partial \psi}{\partial y} = -\frac{1}{\rho_{(f)}} \frac{\partial p}{\partial x} + \frac{\mu_{(CNT)}}{\rho_{(f)}} \left[\frac{\partial^2 \psi}{\partial x^2} + \frac{\partial^2 \psi}{\partial y^2} \right] - \sigma_{(CNT)} (B^*)^2 \psi. \tag{4}$$

$$\frac{\partial \upsilon}{\partial t} + \psi \frac{\partial \upsilon}{\partial x} + \upsilon \frac{\partial \upsilon}{\partial y} = -\frac{1}{\rho_{(f)}} \frac{\partial p}{\partial y} + \frac{\mu_{(CNT)}}{\rho_{(f)}} \left[\frac{\partial^2 \upsilon}{\partial x^2} + \frac{\partial^2 \upsilon}{\partial y^2} \right] \tag{5}$$

Joule heating and viscous dissipation energy equations given as,

$$\begin{aligned} \frac{\partial \xi}{\partial t} + \psi \frac{\partial \xi}{\partial x} + \upsilon \frac{\partial \xi}{\partial y} = {} & \frac{\kappa^*_{(CNT)}}{(\rho c_p)_{(f)}} \left[\frac{\partial^2 \xi}{\partial x^2} + \frac{\partial^2 \xi}{\partial y^2} \right] + \frac{\sigma_{(CNT)} (B^*)^2}{(\rho c_p)_{(f)}} (\psi^2 \\ & + \upsilon^2) + \frac{2\mu_{(CNT)}}{(\rho c_p)_{(f)}} \left[(\frac{\partial^2 \psi}{\partial x})^2 + (\frac{\partial \upsilon}{\partial y})^2 + (\frac{\partial \upsilon}{\partial x} + \frac{\partial \psi}{\partial y})^2 \right] - \frac{2}{3} \left[\frac{\partial \psi}{\partial x} + \frac{\partial \upsilon}{\partial y} \right]^2 \end{aligned} \tag{6}$$

Similarly equations for homogeneous and heterogeneous forms as,

$$\frac{\partial a^*}{\partial t} + \psi \frac{\partial a^*}{\partial x} + \upsilon \frac{\partial a^*}{\partial y} = D_\Omega \frac{\partial^2 a^*}{\partial y^2} - K^*_c a^* (b^*)^2. \tag{7}$$

$$\frac{\partial b^*}{\partial t} + \psi \frac{\partial b^*}{\partial x} + \upsilon \frac{\partial b^*}{\partial y} = D^*_B \frac{\partial^2 b^*}{\partial y^2} + K^*_c a^* (b^*)^2. \tag{8}$$

For the following equations, we used ψ, υ shows the recursive components of the horizontal and vertical velocity components of nanofluid, where fluid pressure is p, temperature distribution is ξ and the homogeneous and heterogeneous response variables are a^* and b^*. The effective fluid density is expressed in terms of ρ. The heat capacity of the fluid is ρc_p, and its electrical conductivity for carbon nanotubes nanofluid is σ_{CNT}. The chemical species associated with B^* and Ω, diffusion coefficients are displayed by the variables D_Ω and D^*_B respectively. Thermal conductivity for carbon nanotubes nanofluid by κ_{CNT}.

3. Similarity Transformation Approach For Boundary Conditions

The following criteria were established for the problem's boundaries:

$$\begin{aligned} & \psi = 0, \quad \upsilon = 0, \quad \xi = \xi_l, \quad D_\Omega \frac{\partial a^*}{\partial y} = \Gamma_2 a^*, \quad D^*_B \frac{\partial b^*}{\partial y} = -\Gamma_2 a^*, \qquad at \quad y = 0. \\ & \psi = 0, \quad \upsilon = \frac{-\alpha D}{2\sqrt{1-\alpha t}}, \quad \xi = \xi_\psi, \quad a^* = a^*_0, \quad b^* = 0, \qquad at \quad y = h(t). \end{aligned} \tag{9}$$

The following similarity transformations technique [31] was used to convert the differential equations system into the system of ordinary differential equations.

$$\psi = \frac{\alpha x \Phi'(\Upsilon)}{2(1-\alpha t)},\ \ \upsilon = \frac{-\alpha l \Phi(\Upsilon)}{2\sqrt{1-\alpha t}},\ \ \xi = \vartheta(\Upsilon)\xi_j,\ \ \Upsilon = \frac{y}{l\sqrt{1-\alpha t}},$$

and

$$a^* = a_0^* \Phi(\Upsilon),\ \ b^* = a_0^*(\Upsilon),\ \ B^*(t) = \frac{B_0^*}{\sqrt{1-\alpha t}},\ \ \vartheta = \frac{\xi - \xi_i}{\xi_j - \xi_i}.$$

There is an identical satisfaction of the continuity equation (3). The equations of momentum, temperature distribution, homogeneous and heterogeneous chemical reactions, is as follows

$$\Phi'''' - S_r \frac{A_4}{A_1}\left(\Phi''\Phi' + 2\Phi'' - \Phi\Phi''' + \Upsilon\Phi'''\right) - \frac{A_5}{A_1}\Phi(a^*)^2\Phi'' = 0. \tag{10}$$

$$\frac{A_3}{A_1}\vartheta'' - P_r^* S_r\left(\Upsilon\vartheta' - \Phi\vartheta' - \frac{A_5}{A_2}ME_1\Phi'^2 - \frac{A_1}{A_2}2NE_2\Phi'^2 - \frac{A_1}{A_2}NE_1\delta\Phi''^2 - \frac{A_5}{A_2}\frac{ME_2}{\delta}\Phi^2\right) = 0. \tag{11}$$

$$\varphi'' - 2S_r S_c^*\left(\Upsilon\varphi' - \Phi\varphi' + \Gamma_1\varphi^2\right) = 0. \tag{12}$$

$$''\beta - S_r S_c^*\left(\Upsilon' - \Phi' - \Gamma_1\varphi^2\right) = 0. \tag{13}$$

The following outcome will be obtained by substituting Ai for the dimensionless constant. $A_1 = \frac{(\mu)_{CNT}}{\mu_f}$, $A_2 = \frac{(\rho C_p)_{CNT}}{(\rho C_p)_f}$, $A_3 = \frac{(\kappa)_{CNT}}{\kappa_f}$, $A_4 = \frac{(\rho)_{CNT}}{\rho_f}$, $A_5 = \frac{\kappa_{CNT}}{\rho C_p}$.
Likewise, the similarities transformation of the boundary circumstances change to,

$$\begin{aligned} &\Phi(0) = 0,\ \ \Phi'(0) = 0,\ \ \vartheta(0) = 1,\ \ \varphi'(0) = \Gamma_2\varphi(0),\ \ \beta'(0) = -\Gamma_2\varphi(0). \\ &\Phi(1) = 1/2,\ \ \Phi'(1) = 0,\ \ \vartheta(1) = 0,\ \ \varphi(1) = 1\ \ \ (1) = 0, \end{aligned} \tag{14}$$

In the case of carbon nanotubes, the squeezed Reynolds number is $S_r = \frac{\alpha l^2}{2\nu_{(f)}}$, the Hartman parameter is $\varphi a* = lB_0^*\sqrt{\frac{\sigma_{(CNT)}}{\mu_{(f)}}}$, the Prandtl parameter is $P_r^* = \frac{(\mu c_p)_{(CNT)}}{\kappa_{(f)}}$, Schmidt number is $S_c^* = \frac{v_{(CNT)}}{D_\Omega}$, Homogeneous reaction strength is $\Gamma_1 = \frac{2(\kappa_c)_{(CNT)}(a_0^*)^2(1-\alpha t)}{\alpha}$ and the heterogeneous reaction strength is $\Gamma_2 = \frac{(\kappa_s)_{(CNT)}}{D_\Omega}$, local Eckert number is$E_1 = \frac{\alpha^2 x^2}{\xi_l(1-\alpha t)^2}$, Eckert number is $E_2 = \frac{\alpha^2}{\xi_l(1-\alpha t)}$, magnetic field parameter is $M = \frac{\sigma_{(CNT)}(B_0^*)^2}{2(\rho C_p)_{(f)}\alpha}$, porosity number is $N = \frac{\mu_{(CNT)}}{(\rho C_p)_{(f)}\alpha}$, $\delta = \frac{1}{l^2}$ is a small parameter, and $\beta = \frac{D_\Omega}{D_B^*}$ represents the diffusion coefficient ratio. Here, we presume that Ω and B^* are the coefficients of diffusion for chemical species of identical sizes.The alternative theory states that D_Ω and D_{B^*} are comparable; hence, $\beta = \frac{D_\Omega}{D_B^*} = 1$; also, $(\Upsilon) + \varphi(\Upsilon) = 1$ [32],

Constants of Study

In engineering, among the coefficients of importance are the skin friction coefficient (C_{Φ}), the Sherwood number ($S_r h$), and the local Nusselt number ($N\psi$)..
$C^*_{\Phi} = \frac{S_r}{h} C_{\Phi} = \Phi''(0)$, $-\vartheta'(0) = N\psi$, $-'(0) = -\varphi'(0) = S_r h$.
The outcome when A_i is used as the dimensionless constant is as follows:

$$A_1 = \frac{(\mu)_{CNT}}{\mu_f} = \frac{\mu_f}{(1-\phi_1)^{2.5}(1-\phi_2)^{2.5}}. \tag{15}$$

$$A_2 = \frac{(\rho C_p)_{CNT}}{(\rho C_p)_f} = (1-\phi_2)\left[(1-\phi_1)(\rho C_p)_{CNT} + \phi_1(\rho C_p)_1\right] + \phi_2(\rho C_p)_2. \tag{16}$$

$$A_3 = \frac{(\kappa)_{CNT}}{\kappa_f} = \frac{(\kappa_1+\kappa_2) + (1-\phi_1)\kappa_f + 2\phi_1\kappa_1 + 2\phi_2\kappa_2}{(\kappa_1+\kappa_2) + (1+\phi_1)\kappa_f + (\phi_1\kappa_1 + \phi_2\kappa_2)}. \tag{17}$$

$$A_4 = \frac{\rho_{CNT}}{\rho_f} = (1-\phi_2)\left[(1-\phi_1)(\rho_f) + \phi_1\rho_1\right] + \phi_2\rho_2. \tag{18}$$

$$A_5 = \sigma_{nf} = \frac{(\kappa)_{CNT}}{(\rho C_p)_f}. \tag{19}$$

The volume fractions of the carbon nanotubes nanoparticles are expressed by the symbols $\phi 1$ and $\phi 2$, while the density of carbon nanotubes, nanofluid Alumina and base fluids, are expressed by ρ_1, ρ_2 and ρ_f respectively, and electrical conductivity of carbon nanotubes and for base fluids of nanoparticales are expressed by σ_1, σ_2 and σ_f.

Table 1: Thermo physical properties of carbon nanotubes nanoparticales (Alumina) and Ethylene-glycol with water at 20^oC.

Physical properties	$\rho\left(\frac{kg}{m^3}\right)$	$c_p\left(\frac{J}{kgK}\right)$	$k\left(\frac{W}{mK}\right)$	$\sigma\left(sm^{-1}\right)$
$C_2H_6O_2 + H_2O$	1063.8	3630	0.387	1×10^{-7}
Single wall carbon nanotubes	2600	425	6600	0.00597
Multi wall carbon nanotubes	1600	796	300	2.3×10^{-5}
Alumina	3970	765	40	1.3×10^{-5}

4. Approximate Analytical Solution

Homotopy analysis method analysis was utilized to solve the system of equations (10 − 13). As a result of Homotopy analysis method, a collection of base functions Υ^c, $c \geq 0$ may be used to organize the functions $\Phi(\Upsilon)$, $\vartheta(\Upsilon)$, $\varphi(\Upsilon)$, and (Υ) respectively.

$$\Phi_{\Psi}() = \sum_{\pounds=0}^{\infty} a^*_{\pounds}{}^{\pounds}, \tag{20}$$

$$\vartheta_{\Psi}() = \sum_{\pounds=0}^{\infty} b^*_{\pounds}{}^{\pounds}, \tag{21}$$

$$\varphi_{\Psi}() = \sum_{\pounds=0}^{\infty} c^*_{\pounds}{}^{\pounds}, \tag{22}$$

$$_{\Psi}() = \sum_{\pounds=0}^{\infty} d^*_{\pounds}{}^{\pounds}, \tag{23}$$

That is, the constant coefficients that we need to be found are $a^*_{\pounds}$, $b^*_{\pounds}$, $c^*_{\pounds}$ and $d^*_{\pounds}$. We choose the following initial approximations:

$$\Phi_0() = \frac{3}{2}{}^2 - {}^3, \tag{24}$$

$$\vartheta_0() = 1 - , \tag{25}$$

$$\varphi_0() = (1 + \Gamma^*_2)/(1 + \Gamma^*_2), \tag{26}$$

$$_0() = (\Gamma^*_2 - \Gamma^*_2)/(1 + \Gamma^*_2\beta). \tag{27}$$

The auxiliary operators are chosen as

$$\ell_{\Phi} = \frac{\partial^4}{\partial^4}, \quad \ell_{\vartheta} = \frac{\partial^2}{\partial^2}, \quad \ell_{\varphi} = \frac{\partial^2}{\partial^2}, \quad \ell = \frac{\partial^2}{\partial^2}, \tag{28}$$

with the following properties

$$\ell_{\Phi}(\pounds_1{}^3 + \pounds_2{}^2 + \pounds_3 + \xi_4) = 0, \tag{29}$$

$$\ell_{\vartheta}(\pounds_5 + \pounds_6) = 0, \tag{30}$$

$$\ell_{\varphi}(\pounds_7 + \pounds_8) = 0, \tag{31}$$

$$\ell(\pounds_9 + \pounds_{10}) = 0, \tag{32}$$

where $\pounds_1$, $\pounds_2$, $\pounds_3$, $\pounds_4$, $\pounds_5$, $\pounds_6$, $\pounds_7$, $\pounds_8$, $\pounds_9$ and $\pounds_{10}$ are arbitrary constants.
Deformation problems of *zeroth* order as follow:

$$(1;\Upsilon)\ell_{\Phi}[\bar{\Phi}(;\Upsilon) - \Phi_0()] = q\hbar_{\Phi}N_{\Phi}[\bar{\Phi}(;\Upsilon), \bar{\vartheta}(;\Upsilon), \bar{m}(;\Upsilon), \bar{n}(;\Upsilon)], \tag{33}$$

$$(1;\Upsilon)\ell_{\vartheta}[\bar{\vartheta}(;\Upsilon) - \vartheta_0()] = q\hbar_{\vartheta}N_{\vartheta}[\bar{\Phi}(;\Upsilon), \bar{\vartheta}(;\Upsilon), \bar{m}(;\Upsilon), \bar{n}(;\Upsilon)], \tag{34}$$

$$(1;\Upsilon)\ell_{\varphi}[\bar{\varphi}(;\Upsilon) - \varphi_0()] = q\hbar_{\varphi}N_{\varphi}[\bar{\Phi}(;\Upsilon), \bar{\varphi}(;\Upsilon), \bar{}(;\Upsilon)], \tag{35}$$

$$(1;\Upsilon)\ell[\bar{}(;\Upsilon) - _0()] = q\hbar N[\bar{\Phi}(;\Upsilon), \bar{\varphi}(;q), \bar{}(;\Upsilon)]. \tag{36}$$

Given Eqs. $(24-27)$, the nonlinear operators are identified as

$$N_{\Phi}[\bar{\Phi}(;\Upsilon), \bar{\vartheta}(;\Upsilon)] = \frac{\partial^4\bar{\Phi}(;\Upsilon)}{\partial^4} - S_r\frac{A_4}{A_1}\left[\frac{\partial\bar{\Phi}(;\Upsilon)}{\partial}\frac{\partial^2\bar{\Phi}(;\Upsilon)}{\partial^2} + 2\frac{\partial^2\bar{\Phi}(;\Upsilon)}{\partial^2} + \Upsilon\frac{\partial^3\bar{\Phi}(;\Upsilon)}{\partial^3}\right.$$
$$\left. -\Phi\frac{\partial^3\bar{\Phi}(;\Upsilon)}{\partial^3}\right] - \frac{A_5}{A_1}\varphi(a*)^2\frac{\partial^2\bar{\Phi}(;\Upsilon)}{\partial^2}. \tag{37}$$

$$N_{\vartheta}[\bar{\Phi}(;\Upsilon),\bar{\vartheta}(;\Upsilon)] = \frac{A_3}{A_1}\frac{\partial^2\bar{\vartheta}(;\Upsilon)}{\partial^2} - PrS_r\left[\Upsilon\frac{\partial\bar{\vartheta}(;\Upsilon)}{\partial} - \Phi\frac{\partial\bar{\vartheta}(;\Upsilon)}{\partial} - \frac{A_5}{A_2}ME_1\left[\frac{\partial\bar{\Phi}(;\Upsilon)}{\partial}\right]^2 - 2\frac{A_1}{A_2}NE_2\left[\frac{\partial\bar{\Phi}(;\Upsilon)}{\partial}\right]^2 - \frac{A_1}{A_2}NE_1\delta\left[\frac{\partial^2\bar{\Phi}(;\Upsilon)}{\partial^2}\right]^2 - \frac{A_5}{A_2}ME_2\frac{\Phi^2}{\delta}\right],$$

$$N_{\varphi}[\bar{\Phi}(;\Upsilon),\bar{\varphi}(;\Upsilon),\bar{\gamma}(;\Upsilon)] = \frac{\partial^2\bar{\varphi}(;\Upsilon)}{\partial^2} - 2S_c^*S_r\left[\Upsilon\frac{\partial\bar{\varphi}(;\Upsilon)}{\partial} - \Phi\frac{\partial\bar{\varphi}(;\Upsilon)}{\partial} + \Gamma_1\varphi()^2\right], \quad (38)$$

$$N[\bar{\Phi}(;\Upsilon),\bar{\varphi}(;\Upsilon),\bar{\gamma}(;\Upsilon)] = \frac{\partial^2\bar{\gamma}(;\Upsilon)}{\partial^2}\delta - S_c^*S_r\left[\Upsilon\frac{\partial\bar{\gamma}(;\Upsilon)}{\partial} - \Phi\frac{\partial\bar{\gamma}(;\Upsilon)}{\partial} - \Gamma\Phi\frac{\partial\bar{\gamma}(;\Upsilon)}{\partial}\right], \quad (39)$$

The embedding parameter is Υ, the nonzero auxiliary parameters are $\hbar_{\Phi}$, $\hbar_{\vartheta}$, $\hbar_{\varphi}$, and $\hbar$, and the nonlinear parameters are N_{Φ}, N_{ϑ}, N_{φ}, and N.
Given $\Upsilon = 0$ and 1, we obtain

$$\begin{aligned} &\bar{\Phi}(,0) = \Phi_o(), && \bar{\Phi}(,1) = \Phi(),\\ &\bar{\vartheta}(,0) = \vartheta_o(), && \bar{\vartheta}(,1) = \vartheta(),\\ &\bar{\varphi}(,0) = \varphi_o(), && \bar{\varphi}(,1) = \varphi(),\\ &\bar{\gamma}(,0) = {}_o(), && \bar{\gamma}(,1) = (), \end{aligned} \quad (40)$$

Thus, since Υ change between 0 and 1, we may state that $\bar{\Phi}(,0)$, $\bar{\vartheta}(,0)$, $\bar{\varphi}(,0)$, $\bar{\gamma}(,0)$ varies from initial guesses $\Phi_0()$, $\vartheta_0()$, $\varphi_0()$ and ${}_0()$ to exact solution $\Phi()$, $\vartheta()$, $\varphi()$ and $()$ respectively.
After expanding these functions in Taylor's series, we obtain:

$$\Phi(;\Upsilon) = \Phi_0() + \sum_{\Psi=1}^{\infty}\Upsilon^{\Psi}\Phi_{\Psi}(), \quad (41)$$

$$\vartheta(;\Upsilon) = \vartheta_0() + \sum_{\Psi=1}^{\infty}\Upsilon^{\Psi}\vartheta_{\Psi}(), \quad (42)$$

$$\varphi(;\Upsilon) = \varphi_0() + \sum_{\Psi=1}^{\infty}\Upsilon^{\Psi}\varphi_{\Psi}(), \quad (43)$$

$$(;\Upsilon) = {}_0() + \sum_{\Psi=1}^{\infty}\Upsilon^{\Psi}{}_{\Psi}(), \quad (44)$$

$$\Phi_{\Psi}() = \frac{1}{\Psi!}\frac{\partial^{\Psi}\Phi(;\Upsilon)}{\partial^{\Psi}}\bigg|_{\Upsilon=0}, \vartheta_{\Psi}() = \frac{1}{\Psi!}\frac{\partial^{\Psi}\vartheta(;\Upsilon)}{\partial^{\Psi}}\bigg|_{\Upsilon=0}, \varphi_{\Psi}() = \frac{1}{\Psi!}\frac{\partial^{\Psi}\varphi(;\Upsilon)}{\partial^{\Psi}}\bigg|_{\Upsilon=0}, \quad {}_{\Psi}() = \frac{1}{\Psi!}\frac{\partial^{\Psi}(;\Upsilon)}{\partial^{\Psi}}\bigg|_{\Upsilon=0} \quad (45)$$

Note that $\hbar_{\Phi}$, $\hbar_{\vartheta}$ and other factors are very important for the convergence of the aforementioned series $\hbar_{\varphi}$ and $\hbar$. Given that the nonzero auxiliary parameters are selected in a way that ensures the convergence of equations $(41-44)$ at $\Upsilon=1$. We obtain

$$\Phi() = \Phi_0() + \sum_{\Psi=1}^{\infty} \Phi_{\Psi}(), \tag{46}$$

$$\vartheta() = \vartheta_0() + \sum_{\Psi=1}^{\infty} \vartheta_{\Psi}(), \tag{47}$$

$$\varphi() = \varphi_0() + \sum_{\Psi=1}^{\infty} \varphi_{\Psi}(), \tag{48}$$

$$() = {}_0() + \sum_{\Psi=1}^{\infty} {}_{\Psi}(), \tag{49}$$

Differentiating the deformation equations $(33-36)$. After setting $\Upsilon=0$ and calculating $\Psi-times$ with regard to Υ, we have

$$\ell_{\Phi}[\Phi_{\Psi}() - \chi_{\Psi}\Phi_{\Psi-1}()] = \hbar_{\Phi} R_{\Phi,\Psi}(), \tag{50}$$

$$\ell_{\vartheta}[\vartheta_{\Psi}() - \chi_{\Psi}\vartheta_{\Psi-1}()] = \hbar_{\vartheta} R_{g,\Psi}(), \tag{51}$$

$$\ell_{\varphi}[\varphi_{\Psi}() - \chi_{\Psi}\varphi_{\Psi-1}()] = \hbar_{\varphi} R_{\varphi,\Psi}(), \tag{52}$$

$$\ell[{}_{\Psi}() - \chi_{\Psi}{}_{\Psi-1}()] = \hbar_{\phi} R_{,\Psi}(), \tag{53}$$

regards with the boundary conditions,

$$\begin{aligned} &\Phi_{\Psi}(0)=0, \quad \Phi'_{\Psi}(0)=0, \quad \vartheta_{\Psi}(0)=1, \quad \varphi'_{\Psi}(0)=\Gamma_2\varphi(0), \quad \beta'_{\Psi}(0)=-\Gamma_2\varphi(0), \\ &\Phi_{\Psi}(1)=1/2, \quad \Phi'_{\Psi}(1)=0, \quad \vartheta_{\Psi}(1)=0, \quad \varphi_{\Psi}(1)=1, \quad {}'_{\Psi}(1)=0, \end{aligned} \tag{54}$$

where

$$\begin{aligned} R_{\Phi,\Psi}() =& \Phi'''_{\Psi-1}() - S_r\frac{A_4}{A_1}\left[\Upsilon\Phi'''_{\Psi-1}() + 2\Phi''_{\Psi-1}() + \sum_{j=0}^{\Psi-1}\Phi'_j()\Phi''_{\Psi-j-1}() - \sum_{j=0}^{\Psi-1}\Phi_j()\Phi'''_{\Psi-j-1}()\right] \\ &- \frac{A_5}{A_1}\varphi(a^*)^2\Phi''_{\Psi-1}(), \end{aligned} \tag{55}$$

$$\begin{aligned} R_{\vartheta,\Psi}() = (\frac{A_3}{A_1})\vartheta''_{\Psi-1}() - P_r^* S_r\Bigg[\Upsilon\sum_{j=0}^{\Psi-1}\vartheta'_{\Psi-j-1}() - \sum_{j=0}^{\Psi-1}\Phi_j()\vartheta'_{\Psi-j-1}() - (\frac{A_5}{A_2})ME_1\sum_{j=0}^{\Psi-1}(\Phi')^2_{\Psi-j-1}() \\ -(\frac{A_1}{A_2})2NE_2\sum_{j=0}^{\Psi-1}(\Phi')^2_{\Psi-j-1}() - (\frac{A_1}{A_2})NE_1\delta\sum_{j=0}^{\Psi-1}(\Phi'')^2_{\Psi-j-1}() - (\frac{A_5}{A_2})\frac{ME_2}{\delta}\sum_{j=0}^{\Psi-1}(\Phi)^2_{\Psi-j-1}()\Bigg], \end{aligned} \tag{56}$$

$$R_{\varphi,\Psi}() = \varphi''_{\Psi-1}() - 2S_r S_c^* \left[\Upsilon \varphi'_{\Psi-j-1}() + \Gamma_1 \varphi_{\Psi-1}()^2 - \sum_{j=0}^{\Psi-1} \Phi_j() \varphi_{\Psi-j-1}() \right]. \tag{57}$$

$$R_{,\Psi}() = {}''_{\Psi-1}()\beta - S_c^* S_r \left[\Upsilon'_{\Psi-1}() - \sum_{j=0}^{\Psi-1} \Phi_j()'_{\Psi-j-1}() - \Gamma_1 \sum_{j=0}^{\Psi-1} \varphi_j()^2_{\Psi-j-1}() \right] \tag{58}$$

Here $\chi_\Psi = \begin{cases} 1, & i\Phi\ \Psi > 1, \quad \text{where} \\ 0, & \Psi = 1. \end{cases}$

The general solution of $(50-53)$ can be expressed in the following way:

$$\Phi_\Psi() = \int_0 \int_0 \int_0 \int_0 \hbar_\Phi R_{\Phi,\Psi}(z) dz dz dz dz dz + \chi_\Psi \Phi_{\Psi-1} + \pounds_1{}^3 + \pounds_2{}^2 + \pounds_3 + \pounds_4, \tag{59}$$

$$\vartheta_\Psi() = \int_0 \int_0 \hbar_\vartheta R_{\vartheta,\Psi}(z) dz dz + \chi_\Psi \vartheta_{\Psi-1} + \pounds_5 + \pounds_6, \tag{60}$$

$$\varphi_\Psi() = \int_0 \int_0 \hbar_\varphi R_{\varphi,\Psi}(z) dz dz + \chi_\Psi \varphi_{\Psi-1} + \pounds_{11} + \pounds_{12}, \tag{61}$$

$$_\Psi() = \int_0 \int_0 \hbar R_{,\Psi}(z) dz dz + \chi_\Psi {}_{\Psi-1} + \pounds_{13} + \pounds_{14}, \tag{62}$$

Therefore, the actual solution $\Phi()$, $\vartheta()$, $\varphi()$ and $\varphi()$ becomes

$$\Phi() \approx \sum_{n=0}^{\Psi} \Phi_n(), \quad \vartheta() \approx \sum_{n=0}^{\Psi} \vartheta_n(), \quad \varphi() \approx \sum_{n=0}^{\Psi} \varphi_n(), \quad () \approx \sum_{n=0}^{\Psi} {}_n(). \tag{63}$$

4.1. Analysis of convergence control parameters

It is significant to notice that the non-zero auxiliary parameters $\hbar_\Phi$, $\hbar_\vartheta$, $\hbar_\varphi$, and $\hbar$ in the series solutions $(59-62)$. Find out where the homotopy series solutions converge and how quickly they do so. To find the optimal values for $\hbar_\Phi$, $\hbar_\vartheta$, $\hbar_\varphi$, and $\hbar$, Liao (2010)'s "average residual error" was employed.

$$\varepsilon_\Psi^\Phi = \frac{1}{\pounds+1} \sum_{j=0}^{\pounds} \left[N_\Phi \left(\sum_{i=0}^{\Psi} \bar{\Phi}(), \sum_{i=0}^{\Psi} \bar{\vartheta}() \right) \right]^2 d, \tag{64}$$

$$\varepsilon_\Psi^\vartheta = \frac{1}{\pounds+1} \sum_{j=0}^{\pounds} \left[N_\vartheta \left(\sum_{i=0}^{\Psi} \bar{\Phi}(), \sum_{i=0}^{\Psi} \bar{\vartheta}() \right)_{n=jD_u n} \right]^2 d, \tag{65}$$

$$\varepsilon_\Psi^\varphi = \frac{1}{\pounds+1} \sum_{j=0}^{\pounds} \left[N_\varphi \left(\sum_{i=0}^{\Psi} \bar{\Phi}(), \sum_{i=0}^{\Psi} \bar{\varphi}(), \sum_{i=0}^{\Psi} \bar{}() \right)_{n=jD_u n} \right]^2 d, \tag{66}$$

$$\varepsilon_\Psi = \frac{1}{\pounds+1} \sum_{j=0}^{\pounds} \left[N \left(\sum_{i=0}^{\Psi} \bar{\Phi}(), \Upsilon \sum_{i=0}^{\Psi} \bar{\varphi}(), \sum_{i=0}^{\Psi} \bar{}() \right)_{n=jD_u n} \right]^2 d, \tag{67}$$

In light of Liao (2010)

$$\varepsilon_{\Psi}^{t} = \varepsilon_{\Psi}^{\Phi} + \varepsilon_{\Psi}^{\vartheta} + \varepsilon_{\Psi}^{\varphi} + \varepsilon_{\Psi}, \tag{68}$$

This expressed the total squared residual error as ε_{Ψ}^{t}. Using the Mathematica program, the total average squared residual error is reduced (**BVPh** 2.0, 2014).

5. Error Analysis

To guarantee that the residual error is as small as possible while maintaining analytical efficiency, an error analysis is carried out. A numerical and analytical solution is provided by Homotopy analysis method and BVP4C. We do the analysis with a 40th-order approximation. The Mathematica program BVPh 2.0 is also used in this investigation to assess the validity of Homotopy analysis method approaches for maximum residual error 10^{-40}. Regarding the consistency and conformation of the Homotopy analysis method solution, the outcomes are contrasted with the numerical solution of BVP4c using Matlab. Error analyses are displayed in Figures 2-3 for single wall carbon nanotubes and multi wall carbon nanotubes and Tables (1-19) to examine the two approaches' dependability for different levels of physical parameters. Figure 2-3 and Table 2-3 both demonstrate how the maximum average residual errors of carbon nanotubes on $\Phi(\Upsilon)$, $\vartheta(\Upsilon)$, $\varphi(\Upsilon)$, and (Υ) are almost gradually reduced up to the 20th transition series.

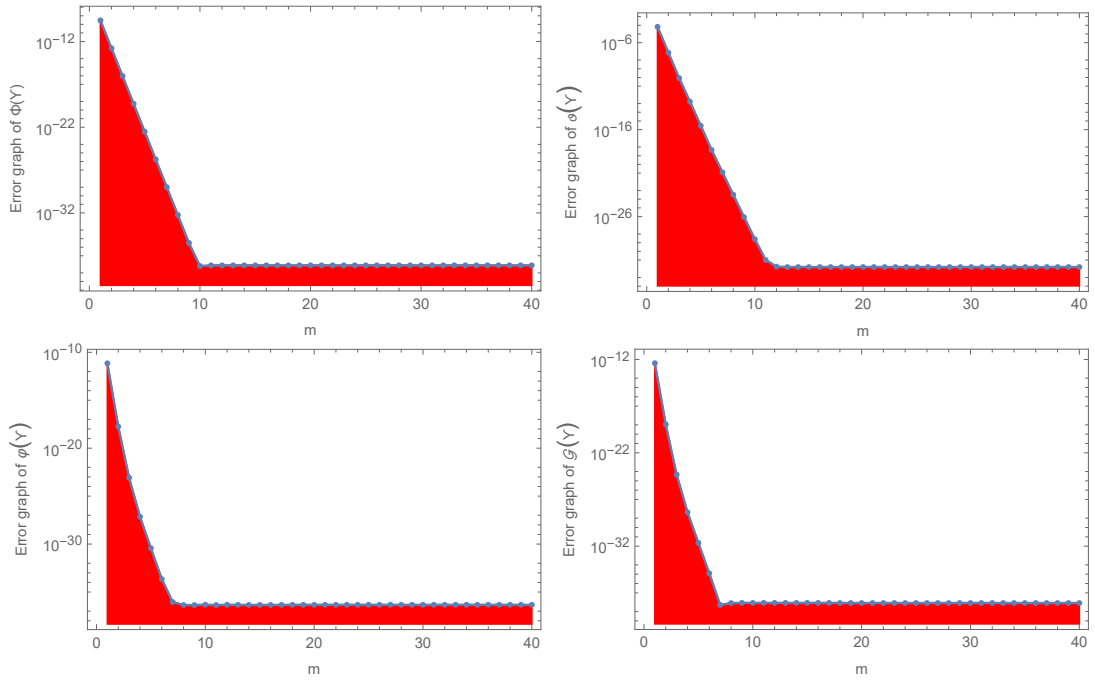

Figure 2: Error analysis of $\Phi(\Upsilon)$, $\vartheta(\Upsilon)$, $\varphi(\Upsilon)$ and (Υ) for Alumina in case of single wall carbon nanotubes with $P_r^* = 4$, $M = 0.2$, $N = 0.3$, $\beta = 0.5$, $S_r = 0.1$, $\delta = 0.1$, $E_1 = 0.1$, $E_2 = 0.2$, $S^*c = 0.1$, $\Gamma 1 = 0.2$, $\Gamma 2 = 0.3$, $\varphi a^* = 0.1$, $\phi 1 = 0.1$, $\phi 2 = 0.2$.

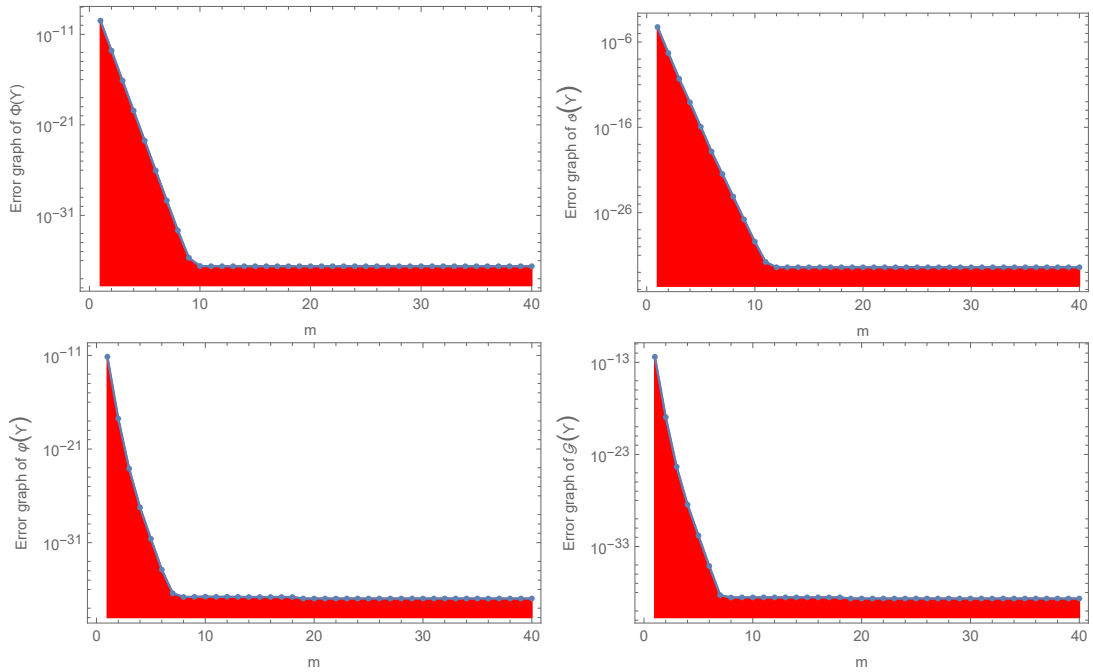

Figure 3: Error analysis of $\Phi(\Upsilon)$, $\vartheta(\Upsilon)$, $\varphi(\Upsilon)$ and (Υ) for Alumina in case of multi wall carbon nanotubes with $P_r^* = 4$, $M = 0.2$, $N = 0.3$, $\beta = 0.5$, $S_r = 0.1$, $\delta = 0.1$, $E_1 = 0.1$, $E_2 = 0.2$, $S^*c = 0.1$, $\Gamma 1 = 0.2$, $\Gamma 2 = 0.3$, $\varphi a^* = 0.1$, $\phi 1 = 0.1$, $\phi 2 = 0.2$.

Table 2: Total residual error of $\Phi(\Upsilon)$, $\vartheta(\Upsilon)$, $\varphi(\Upsilon)$ and (Υ) in case of single wall carbon nanotubes with $P_r^* = 4$, $M = 0.2$, $N = 0.3$, $\beta = 0.5$, $S_r = 0.1$, $\delta = 0.1$, $E_1 = 0.1$, $E_2 = 0.2$, $S^*c = 0.1$, $\Gamma 1 = 0.2$, $\Gamma 2 = 0.3$, $\varphi a^* = 0.1$, $\phi 1 = 0.1$, $\phi 2 = 0.2$.

n	$\epsilon^{\Phi} n$	$\epsilon^{\vartheta} n$	$\epsilon^{\varphi} n$	ϵn
1	2.86053×10^{-10}	0.0000668542	7.0533×10^{-12}	3.98875×10^{-13}
5	3.05126×10^{-23}	2.76859×10^{-16}	3.66382×10^{-31}	2.21904×10^{-32}
10	6.30657×10^{-39}	2.50636×10^{-29}	4.74327×10^{-37}	8.3729×10^{-39}
15	7.57023×10^{-39}	1.58037×10^{-32}	4.47996×10^{-37}	8.3729×10^{-39}
20	7.57023×10^{-39}	1.58037×10^{-32}	4.61396×10^{-37}	8.11943×10^{-39}
25	7.57023×10^{-39}	1.58037×10^{-32}	4.61396×10^{-37}	8.11943×10^{-39}
30	7.57023×10^{-39}	1.58037×10^{-32}	4.61396×10^{-37}	8.11943×10^{-39}
35	7.57023×10^{-39}	1.58037×10^{-32}	4.61396×10^{-37}	8.11943×10^{-39}
40	7.57023×10^{-39}	1.58037×10^{-32}	4.61396×10^{-37}	8.11943×10^{-39}

Table 3: Total residual error of $\Phi(\Upsilon)$, $\vartheta(\Upsilon)$, $\varphi(\Upsilon)$ and (Υ) in case of multi wall carbon nanotubes with $P_r^* = 4$, $M = 0.2$, $N = 0.3$, $\beta = 0.5$, $S_r = 0.1$, $\delta = 0.1$, $E_1 = 0.1$, $E_2 = 0.2$, $S^*c = 0.1$, $\Gamma 1 = 0.2$, $\Gamma 2 = 0.3$, $\varphi a^* = 0.1$, $\phi 1 = 0.1$, $\phi 2 = 0.2$.

n	$\epsilon^{\Phi} n$	$\epsilon^{\vartheta} n$	$\epsilon^{\varphi} n$	ϵn
1	3.19065×10^{-10}	0.0000570536	7.05213×10^{-12}	3.98808×10^{-13}
5	1.81537×10^{-23}	1.14989×10^{-16}	2.59573×10^{-31}	1.57021×10^{-32}
10	2.52521×10^{-37}	3.95875×10^{-30}	1.72533×10^{-37}	2.97937×10^{-39}
15	2.38733×10^{-37}	3.97163×10^{-33}	1.56546×10^{-37}	2.97937×10^{-39}
20	2.38733×10^{-37}	3.97163×10^{-33}	1.08337×10^{-37}	2.24561×10^{-39}
25	7.57023×10^{-39}	1.58037×10^{-32}	4.61396×10^{-37}	8.11943×10^{-39}
30	7.57023×10^{-39}	1.58037×10^{-32}	4.61396×10^{-37}	8.11943×10^{-39}
35	7.57023×10^{-39}	1.58037×10^{-32}	4.61396×10^{-37}	8.11943×10^{-39}
40	7.57023×10^{-39}	1.58037×10^{-32}	4.61396×10^{-37}	8.11943×10^{-39}

Table 4: Computational of multi wall carbon nanotubes nanoparticales (Alumina+Ethylene-glycol with water) for $\Phi(\Upsilon)$, $\vartheta(\Upsilon)$, $\varphi(\Upsilon)$ and (Υ) with $P_r^* = 0.1$, $M = 0.5$, $N = 0.1$, $\beta = 0.7$, $S_r = -0.2$, $\delta = 0.5$, $E_1 = 0.1$, $E_2 = 0.2$, $S^*c = 1.1$, $\Gamma 1 = 0.5$, $\Gamma 2 = -1.3$, $\varphi a^* = 0.1$, $\phi 1 = 0.1$, $\phi 2 = 0.2$.

MWCNT HAM Results					MWCNT Numerical Results			
Υ	$\Phi(\Upsilon)$	$\vartheta(\Upsilon)$	$\varphi(\Upsilon)$	(Υ)	$\Phi(\Upsilon)$	$\vartheta(\Upsilon)$	$\varphi(\Upsilon)$	(Υ)
0	0	1.0000	0.3679	-0.6717	0	1.0000	0.3679	-0.6717
0.1001	0.0139	1.1193	0.4066	-0.6032	0.0139	1.1193	0.4066	-0.6032
0.2002	0.0517	1.2368	0.4494	-0.5347	0.0517	1.2368	0.4494	-0.5347
0.3003	0.1076	1.3481	0.4967	-0.4663	0.1076	1.3481	0.4967	-0.4663
0.4004	0.1755	1.4471	0.5490	-0.3981	0.1755	1.4471	0.5490	-0.3981
0.5005	0.2496	1.5241	0.6068	-0.3302	0.2496	1.5241	0.6068	-0.3302
0.6006	0.3238	1.5639	0.6707	-0.2628	0.3238	1.5639	0.6707	-0.2628
0.7007	0.3920	1.5371	0.7413	-0.1959	0.3920	1.5371	0.7413	-0.1959
0.8008	0.4481	1.3834	0.8194	-0.1297	0.4481	1.3834	0.8194	-0.1297
0.9099	0.4862	0.9682	0.9057	-0.0641	0.4862	0.9682	0.9057	-0.0641
1.0000	0.5000	0	1.0000	0	0.5000	0	1.0000	0

As Υ increases, the values of $\vartheta(\Upsilon)$, and (Υ) drop. Whereas the value of $\Phi(\Upsilon)$, $\varphi(\Upsilon)$ increases as Υ values increase, which is shown in Table 4.

Table 5 shows the values of $\Phi''(0)$, $-\vartheta'(0)$, $-\varphi'(0)$ and $-'(0)$ for various values of Υ. These values are related to the local coefficient of skin friction, the local Nusselt and shewored numbers (homogeneous-heterogeneous reactions).

6. Results and Discussions

This section has been structured to ascertain the effects of various important parameters on the local rates of heat transfer at the squeezing plate surface and the local skin-fraction coefficient, both of which are computed and very significant in terms of physical properties. Equations (14) are obtained by numerically solving the system of non-

Table 5: Computational of multi wall carbon nanotube nanoparticales (Alumina+Ethylene-glycol with water) for $\Phi''(0)$, $-\vartheta'(0)$, $-\varphi'(0)$ and $-'(0)$ with $P_r^* = 0.1$, $M = 0.5$, $N = 0.1$, $\beta = 0.7$, $S_r = -0.2$, $\delta = 0.5$, $E_1 = 0.1$, $E_2 = 0.2$, $S^*c = 1.1$, $\Gamma 1 = 0.5$, $\Gamma 2 = -1.3$, $\varphi a^* = 0.1$, $\phi 1 = 0.3$, $\phi 2 = 0.4$.

MWCNT HAM Results					MWCNT Numerical Results			
Υ	$\Phi''(0)$	$-\vartheta'(0)$	$-\varphi'(0)$	$-'(0)$	$\Phi''(0)$	$-\vartheta'(0)$	$-\varphi'(0)$	$-'(0)$
0	2.9796	0.2800	0.4782	-0.6832	2.9796	0.2800	0.4782	-0.6832
0.1001	2.3881	0.2843	0.4807	-0.6847	2.3881	0.2843	0.4807	-0.6847
0.2002	1.7963	0.3124	0.4813	-0.6843	1.7963	0.3124	0.4813	-0.6843
0.3003	1.2031	0.3819	0.4802	-0.6825	1.2031	0.3819	0.4802	-0.6825
0.4004	0.6076	0.5064	0.4780	-0.6795	0.6076	0.5064	0.4780	-0.6795
0.5005	0.0094	0.6970	0.4747	-0.6757	0.0094	0.6970	0.4747	-0.6757
0.6006	-0.5917	0.9639	0.4704	-0.6710	-0.5917	0.9639	0.4704	-0.6710
0.7007	-1.1961	1.3155	0.4652	-0.6654	-1.1961	1.3155	0.4652	-0.6654
0.8008	-1.8043	1.7563	0.4590	-0.6589	-1.8043	1.7563	0.4590	-0.6589
0.9099	-2.4171	2.2802	0.4515	-0.6511	-2.4171	2.2802	0.4515	-0.6511
1.0000	-3.0294	2.8540	0.4426	-0.6420	-3.0294	2.8540	0.4426	-0.6420

linear equations (10)-(13) for different values of physical parameters. Homotopy analysis method and BVP4C are used in the numerical approach. The current problem has a large number of physical characteristics, which allows for a broad variety of results. The distributions of velocity, temperature distribution, homogeneous and heterogeneous chemical reactions,Joule heating and viscous dissipation are all obtained by solving equations (10)-(13) and are shown in figures 2-13 for different physical parameters. The effect of single wall carbon nanotubes nanoparticles is shown by dashed lines, and the effect of multi wall carbon nanotubes particles is shown by solid lines in the graphs. The Reynolds squeeze parameter governs the strength of squeezing motion, where higher values accelerate the fluid motion and enhance skin friction, directly affecting energy dissipation and lubrication efficiency. The Prandtl number reflects the relative thickness of velocity and thermal boundary layers; higher Pr reduces thermal diffusivity, leading to steeper temperature gradients and stronger heat transfer rates, which is crucial for cooling applications. The Schmidt number characterises the competition between momentum and mass diffusivity; larger values suppress solute penetration into the flow, thereby reducing the thickness of the concentration boundary layer and affecting reaction efficiency. The Eckert number, representing viscous dissipation effects, converts kinetic energy into internal energy, which elevates the fluid temperature and can hinder cooling performance if not controlled. The Lewis number links thermal and mass diffusivities; higher values favour thermal diffusion over mass transport, influencing both heat transfer enhancement and chemical reaction rates. These interpretations are now explicitly connected to practical implications. For example, optimising the squeeze Reynolds number and Prandtl number can enhance cooling performance in microelectromechanical systems and lubrication technologies, while careful control of Schmidt and Lewis numbers can improve mass transfer and reaction efficiency in chemical processing.

The objective of tables (5-7) and (8-19) is to perform a numerical impact test of

different physical parameters. The tables demonstrate that all of the results agree well with the BVP4c and Homotopy analysis method results. It has been shown that the influences of skin friction coefficients, velocity, temperature, Nusselt and Sherwood numbers, and both homogeneous and heterogeneous factors produce an increase in the mass transfer rate. An increase in the internal heat production parameter results in a decrease in the skin friction coefficient and the rate of heat transmission. Increasing the squeezing parameter has been shown to provide a set of outcomes that are comparable. The local Nusselt number and the friction factor decrease when the squeezing parameter is decreased. The skin friction coefficient demonstrated a declining trend, indicating that the floor was drawing the fluid. Tables 2-19 shows the results for $\Phi(\Upsilon)$, $\vartheta(\Upsilon)$, $\varphi(\Upsilon)$ and (Υ) , $\Phi''(0)$, $-\vartheta'(0)$, $-\varphi'(0)$ and $-'(0)$.

Table 6: Computational for single wall carbon nanotubes nano-particales and multi wall carbon nanotube hybrid nano-particales in case of skin friction $\Phi''(0)$.

Various fluid model parameters				SWCNT Nano particals	MWCNT Hybrid nano particals
S_r	φa^*	ϕ_1	ϕ_2	$\Phi''(0)$	$\Phi''(0)$
0.1	0.01	0.1	0.2	3.0471	3.0214
-0.1				3.0048	2.9786
-0.3				2.9618	2.9352
	0.01			2.9834	2.9570
	0.05			3.5653	2.9596
	0.1			4.9633	2.9679
		0.1		2.9834	2.9813
		0.2		2.9924	2.9813
		0.3		3.0064	2.9812
			0.1	2.9816	2.9570
			0.4	2.9962	2.9571
			0.7	3.0444	2.9579

Table 7: Computational for single wall carbon nanotubes nano-particales and multi wall carbon nanotube hybrid nano-particales in case of Nustlt Number $-\vartheta'(0)$.

Various fluid model parameters							SWCNT Nano particals	MWCNT Hybrid nano particals
S_r	P_r^*	ϕ_1	ϕ_2	N	E_1	E_2	$-\vartheta'(0)$	$-\vartheta'(0)$
0.1	0.1	0.1	0.2	0.1	0.1	0.2	2.3096	2.3093
-0.1							-0.3586	-0.3595
-0.3							-1.5130	-1.5159
	0.1						-1.1924	-1.1945
	0.2						-1.6217	-1.6250
	0.3						-1.7025	-1.7061
		0.1					-1.6584	-1.1945
		0.3					-1.6375	-0.4360
		0.5					-1.5889	0.3422
			0.1				-1.4184	-1.1945
			0.4				-0.2952	-0.2960
			0.7				0.8333	0.8332
				0.1			-1.1924	-1.1945
				0.5			-1.1923	-1.1944
				1			-1.1922	-1.1943
					0.1		-1.1924	-1.1945
					0.4		-1.1923	-1.1943
					0.8		-1.1921	-1.1942
						0.2	-1.1924	-1.1945
						0.4	-1.1923	-1.1944
						0.7	-1.1922	-1.1943

Table 8: Computational of multi wall carbon nanotubes nanoparticales (Alumina+Ethylene-glycol with water) for different values of S_r on $\Phi''(0)$, $-\vartheta'(0)$, $-\varphi'(0)$ and $-'(0)$ with $P_r^* = 0.1$, $M = 0.5$, $N = 0.1$, $\beta = 0.7$, $\delta = 0.1$, $E_1 = 0.1$, $E_2 = 0.2$, $S^*c = 0.1$, $\Gamma 1 = 0.5$, $\Gamma 2 = -1.3$, $\varphi a^* = 0.01$, $\phi 1 = 0.1$, $\phi 2 = 0.2$

MWCNT HAM Results					MWCNT Numerical Results			
S_r	$\Phi''(0)$	$-\vartheta'(0)$	$-\varphi'(0)$	$-'(0)$	$\Phi'(0)$	$-\vartheta'(0)$	$-\varphi'(0)$	$-''(0)$
-0.2	2.9570	-1.1945	0.4782	-0.6832	2.9570	-1.1945	0.4782	-0.6832
-0.4	2.9133	-1.6300	0.4782	-0.6832	2.9133	-1.6300	0.4782	-0.6832
-0.6	2.8689	-1.7166	0.4782	-0.6832	2.8689	-1.7166	0.4782	-0.6832
-0.8	2.8238	-1.7613	0.4782	-0.6832	2.8238	-1.7613	0.4782	-0.6832

Table 9: Computational of multi wall carbon nanotubes nanoparticales (Alumina+Ethylene-glycol with water) for different values of P_r^* on $\Phi''(0)$, $-\vartheta'(0)$, $-\varphi'(0)$ and $-'(0)$ with $S_r = -0.2$, $M = 0.5$, $N = 0.1$, $\beta = 0.7$, $\delta = 0.1$, $E_1 = 0.1$, $E_2 = 0.2$, $S^*c = 0.1$, $\Gamma 1 = 0.5$, $\Gamma 2 = -1.3$, $\varphi a^* = 0.01$, $\phi 1 = 0.1$, $\phi 2 = 0.2$

MWCNT HAM Results					MWCNT Numerical Results			
P_r^*	$\Phi''(0)$	$-\vartheta'(0)$	$-\varphi'(0)$	$-'(0)$	$\Phi'(0)$	$-\vartheta'(0)$	$-\varphi'(0)$	$-''(0)$
0.1	2.9570	-1.1945	0.4782	-0.6832	2.9570	-1.1945	0.4782	-0.6832
0.2	2.9570	-1.6250	0.4782	-0.6832	2.9570	-1.6250	0.4782	-0.6832
0.3	2.9570	-1.7061	0.4782	-0.6832	2.9570	-1.7061	0.4782	-0.6832
0.4	2.9570	-1.7455	0.4782	-0.6832	2.9570	-1.7455	0.4782	-0.6832

Table 10: Computational of multi wall carbon nanotubes nanoparticales (Alumina+Ethylene-glycol with water) for different values of E_1 on $\Phi''(0)$, $-\vartheta'(0)$, $-\varphi'(0)$ and $-'(0)$ with $S_r = -0.2$, $P_r^* = 0.1$, $M = 0.5$, $N = 0.1$, $\beta = 0.7$, $\delta = 0.1$, $E_2 = 0.2$, $S^*c = 0.1$, $\Gamma 1 = 0.5$, $\Gamma 2 = -1.3$, $\varphi a^* = 0.01$, $\phi 1 = 0.1$, $\phi 2 = 0.2$.

MWCNT HAM Results					MWCNT Numerical Results			
E_1	$\Phi''(0)$	$-\vartheta'(0)$	$-\varphi'(0)$	$-'(0)$	$\Phi'(0)$	$-\vartheta'(0)$	$-\varphi'(0)$	$-''(0)$
0.1	2.9570	-1.1945	0.4782	-0.6832	2.9570	-1.1945	0.4782	-0.6832
0.2	2.9570	-1.1944	0.4782	-0.6832	2.9570	-1.1944	0.4782	-0.6832
0.3	2.9570	-1.1944	0.4782	-0.6832	2.9570	-1.1944	0.4782	-0.6832
0.4	2.9570	-1.1943	0.4782	-0.6832	2.9570	-1.1943	0.4782	-0.6832

Table 11: Computational of multi wall carbon nanotubes nanoparticales (Alumina+Ethylene-glycol with water) for different values of E_2 on $\Phi''(0)$, $-\vartheta'(0)$, $-\varphi'(0)$ and $-'(0)$ with $S_r = -0.2$, $P_r^* = 0.1$, $M = 0.5$, $N = 0.1$, $\beta = 0.7$, $\delta = 0.1$, $E_1 = 0.1$, $S^*c = 0.1$, $\Gamma 1 = 0.5$, $\Gamma 2 = -1.3$, $\varphi a^* = 0.01$, $\phi 1 = 0.1$, $\phi 2 = 0.2$.

MWCNT HAM Results					MWCNT Numerical Results			
E_2	$\Phi''(0)$	$-\vartheta'(0)$	$-\varphi'(0)$	$-'(0)$	$\Phi'(0)$	$-\vartheta'(0)$	$-\varphi'(0)$	$-''(0)$
0.2	2.9570	-1.1945	0.4782	-0.6832	2.9570	-1.1945	0.4782	-0.6832
0.3	2.9570	-1.1944	0.4782	-0.6832	2.9570	-1.1944	0.4782	-0.6832
0.5	2.9570	-1.1943	0.4782	-0.6832	2.9570	-1.1943	0.4782	-0.6832
0.8	2.9570	-1.1942	0.4782	-0.6832	2.9570	-1.1942	0.4782	-0.6832

Table 12: Computational of multi wall carbon nanotubes nanoparticales (Alumina+Ethylene-glycol with water) for different values of δ on $\Phi''(0)$, $-\vartheta'(0)$, $-\varphi'(0)$ and $-'(0)$ with $S_r = -0.2$, $P_r^* = 0.1$, $M = 0.5$, $N = 0.1$, $\beta = 0.7$, $\delta = 0.1$, $E_1 = 0.1$, $E_2 = 0.2$, $S^*c = 0.1$, $\Gamma 1 = 0.5$, $\Gamma 2 = -1.3$, $\varphi a^* = 0.01$, $\phi 1 = 0.1$, $\phi 2 = 0.2$.

MWCNT HAM Results					MWCNT Numerical Results			
δ	$\Phi''(0)$	$-\vartheta'(0)$	$-\varphi'(0)$	$-'(0)$	$\Phi'(0)$	$-\vartheta'(0)$	$-\varphi'(0)$	$-''(0)$
0.1	2.9570	-1.1945	0.4782	-0.6832	2.9570	-1.1945	0.4782	-0.6832
-2	2.9570	-1.1946	0.4782	-0.6832	2.9570	-1.1946	0.4782	-0.6832
-4	2.9570	-1.1947	0.4782	-0.6832	2.9570	-1.1947	0.4782	-0.6832
-6	2.9570	-1.1948	0.4782	-0.6832	2.9570	-1.1948	0.4782	-0.6832

Table 13: Computational of multi wall carbon nanotubes nanoparticales (Alumina+Ethylene-glycol with water) for different values of N on $\Phi''(0)$, $-\vartheta'(0)$, $-\varphi'(0)$ and $-'(0)$ with $S_r = -0.2$, $P_r^* = 0.1$, $M = 0.5$, $\delta = 0.1$, $\beta = 0.7$, $\delta = 0.1$, $E_1 = 0.1$, $E_2 = 0.2$, $S^*c = 0.1$, $\Gamma 1 = 0.5$, $\Gamma 2 = -1.3$, $\varphi a^* = 0.01$, $\phi 1 = 0.1$, $\phi 2 = 0.2$.

MWCNT HAM Results					MWCNT Numerical Results			
N	$\Phi''(0)$	$-\vartheta'(0)$	$-\varphi'(0)$	$-'(0)$	$\Phi'(0)$	$-\vartheta'(0)$	$-\varphi'(0)$	$-''(0)$
0.1	2.9570	-1.1945	0.4782	-0.6832	2.9570	-1.1945	0.4782	-0.6832
0.3	2.9570	-1.1944	0.4782	-0.6832	2.9570	-1.1944	0.4782	-0.6832
0.8	2.9570	-1.1943	0.4782	-0.6832	2.9570	-1.1943	0.4782	-0.6832
1.4	2.9570	-1.1942	0.4782	-0.6832	2.9570	-1.1942	0.4782	-0.6832

Table 14: Computational of multi wall carbon nanotubes nanoparticales (Alumina+Ethylene-glycol with water) for different values of φa^* on $\Phi''(0)$, $-\vartheta'(0)$, $-\varphi'(0)$ and $-'(0)$ with $S_r = -0.2$, $P_r^* = 0.1$, $M = 0.5$, $\delta = 0.1$, $\beta = 0.7$, $\delta = 0.1$, $E_1 = 0.1$, $E_2 = 0.2$, $S^*c = 0.1$, $\Gamma 1 = 0.5$, $\Gamma 2 = -1.3$, $N = 0.1$, $\phi 1 = 0.1$, $\phi 2 = 0.2$.

MWCNT HAM Results					MWCNT Numerical Results			
φa^*	$\Phi''(0)$	$-\vartheta'(0)$	$-\varphi'(0)$	$-'(0)$	$\Phi'(0)$	$-\vartheta'(0)$	$-\varphi'(0)$	$-''(0)$
0.1	2.9679	-1.1936	0.4782	-0.6832	2.9679	-1.1936	0.4782	-0.6832
0.2	3.0006	-1.1910	0.4782	-0.6832	3.0006	-1.1910	0.4782	-0.6832
0.3	3.0546	-1.1869	0.4782	-0.6832	3.0546	-1.1869	0.4782	-0.6832
0.4	3.1286	-1.1812	0.4782	-0.6832	3.1286	-1.1812	0.4782	-0.6832

Table 15: Computational of multi wall carbon nanotubes nanoparticales (Alumina+Ethylene-glycol with water) for different values of ϕ_1 on $\Phi''(0)$, $-\vartheta'(0)$, $-\varphi'(0)$ and $-'(0)$ with $S_r = -0.2$, $P_r^* = 0.1$, $M = 0.5$, $\delta = 0.1$, $\beta = 0.7$, $\delta = 0.1$, $E_1 = 0.1$, $E_2 = 0.2$, $S^*c = 0.1$, $\Gamma 1 = 0.5$, $\Gamma 2 = -1.3$, $N = 0.1$, $\phi 2 = 0.2$, $\varphi a^* = 0.1$.

MWCNT HAM Results					MWCNT Numerical Results			
ϕ_1	$\Phi''(0)$	$-\vartheta'(0)$	$-\varphi'(0)$	$-'(0)$	$\Phi'(0)$	$-\vartheta'(0)$	$-\varphi'(0)$	$-''(0)$
0.1	2.9679	-1.1936	0.4782	-0.6832	2.9679	-1.1936	0.4782	-0.6832
0.2	2.9716	-0.8503	0.4782	-0.6832	2.9716	-0.8503	0.4782	-0.6832
0.3	2.9775	-0.4353	0.4782	-0.6832	2.9775	-0.4353	0.4782	-0.6832
0.4	2.9871	-0.0187	0.4782	-0.6832	2.9871	-0.0187	0.4782	-0.6832

Table 16: Computational of multi wall carbon nanotubes nanoparticales (Alumina+Ethylene-glycol with water) for different values of ϕ_2 on $\Phi''(0)$, $-\vartheta'(0)$, $-\varphi'(0)$ and $-'(0)$ with $S_r = -0.2$, $P_r^* = 0.1$, $M = 0.5$, $\delta = 0.1$, $\beta = 0.7$, $\delta = 0.1$, $E_1 = 0.1$, $E_2 = 0.2$, $S^*c = 0.1$, $\Gamma 1 = 0.5$, $\Gamma 2 = -1.3$, $N = 0.1$, $\phi 1 = 0.1$, $\varphi a^* = 0.1$.

MWCNT HAM Results					MWCNT Numerical Results			
ϕ_2	$\Phi''(0)$	$-\vartheta'(0)$	$-\varphi'(0)$	$-'(0)$	$\Phi'(0)$	$-\vartheta'(0)$	$-\varphi'(0)$	$-''(0)$
0.1	2.9727	-1.4207	0.4782	-0.6832	2.9727	-1.4207	0.4782	-0.6832
0.2	2.9679	-1.1936	0.4782	-0.6832	2.9679	-1.1936	0.4782	-0.6832
0.3	2.9675	-0.8044	0.4782	-0.6832	2.9675	-0.8044	0.4782	-0.6832
0.4	2.9690	-0.2957	0.4782	-0.6832	2.9690	-0.2957	0.4782	-0.6832

Table 17: Computational of multi wall carbon nanotubes nanoparticales (Alumina+Ethylene-glycol with water) for different values of Γ_2 on $\Phi''(0)$, $-\vartheta'(0)$, $-\varphi'(0)$ and $-'(0)$ with $S_r = -0.2$, $P_r^* = 0.1$, $M = 0.5$, $\delta = 0.1$, $\beta = 0.7$, $\delta = 0.1$, $E_1 = 0.1$, $E_2 = 0.2$, $S^*c = 0.1$, $\Gamma 1 = 0.5$, $N = 0.1$, $\phi 1 = 0.1$, $\phi 2 = 0.2$, $\varphi a^* = 0.1$.

MWCNT HAM Results					MWCNT Numerical Results			
Γ_2	$\Phi''(0)$	$-\vartheta'(0)$	$-\varphi'(0)$	$-'(0)$	$\Phi'(0)$	$-\vartheta'(0)$	$-\varphi'(0)$	$-''(0)$
-1.3	2.9690	-0.2957	0.4782	-0.6832	2.9690	-0.2957	0.4782	-0.6832
0.1	2.9690	-0.2957	-0.0368	0.0526	2.9690	-0.2957	-0.0368	0.0526
0.3	2.9690	-0.2957	-0.1104	0.1577	2.9690	-0.2957	-0.1104	0.1577
0.5	2.9690	-0.2957	-0.1839	0.2628	2.9690	-0.2957	-0.1839	0.2628

Table 18: Computational of multi wall carbon nanotubes nanoparticales (Alumina+Ethylene-glycol with water) for different values of β on $\Phi''(0)$, $-\vartheta'(0)$, $-\varphi'(0)$ and $-'(0)$ with $S_r = -0.2$, $P_r^* = 0.1$, $M = 0.5$, $\delta = 0.1$, $\delta = 0.1$, $E_1 = 0.1$, $E_2 = 0.2$, $S^*c = 0.1$, $\Gamma_1 = 0.5$ $\Gamma 2 = -1.3$, $N = 0.1$, $\phi 1 = 0.1$, $\phi 2 = 0.2$, $\varphi a^* = 0.1$.

MWCNT HAM Results					MWCNT Numerical Results			
β	$\Phi''(0)$	$-\vartheta'(0)$	$-\varphi'(0)$	$-'(0)$	$\Phi'(0)$	$-\vartheta'(0)$	$-\varphi'(0)$	$-''(0)$
0.1	2.9690	-0.2957	-0.1839	1.8394	2.9690	-0.2957	-0.1839	1.8394
0.3	2.9690	-0.2957	-0.1839	0.6131	2.9690	-0.2957	-0.1839	0.6131
0.5	2.9690	-0.2957	-0.1839	0.3679	2.9690	-0.2957	-0.1839	0.3679
0.7	2.9690	-0.2957	-0.1839	0.2628	2.9690	-0.2957	-0.1839	0.2628

Table 19: Computational of multi wall carbon nanotubes nanoparticales (Alumina+Ethylene-glycol with water) for different values of M on $\Phi''(0)$, $-\vartheta'(0)$, $-\varphi'(0)$ and $-'(0)$ with $S_r = -0.2$, $P_r^* = 0.1$, $\delta = 0.1$, $\delta = 0.1$, $E_1 = 0.1$, $E_2 = 0.2$, $S^*c = 0.1$, $\Gamma_1 = 0.5$ $\Gamma 2 = -1.3$, $N = 0.1$, $\beta = 0.7$, $\phi 1 = 0.1$, $\phi 2 = 0.2$, $\varphi a^* = 0.1$.

MWCNT HAM Results					MWCNT Numerical Results			
M	$\Phi''(0)$	$-\vartheta'(0)$	$-\varphi'(0)$	$-'(0)$	$\Phi'(0)$	$-\vartheta'(0)$	$-\varphi'(0)$	$-''(0)$
0.5	2.9690	-0.2957	-0.1839	0.2628	2.9690	-0.2957	-0.1839	0.2628
0.7	2.9690	-0.2956	-0.1839	0.2628	2.9690	-0.2956	-0.1839	0.2628
1.5	2.9690	-0.2955	-0.1839	0.2628	2.9690	-0.2955	-0.1839	0.2628
2.6	2.9690	-0.2953	-0.1839	0.2628	2.9690	-0.2953	-0.1839	0.2628

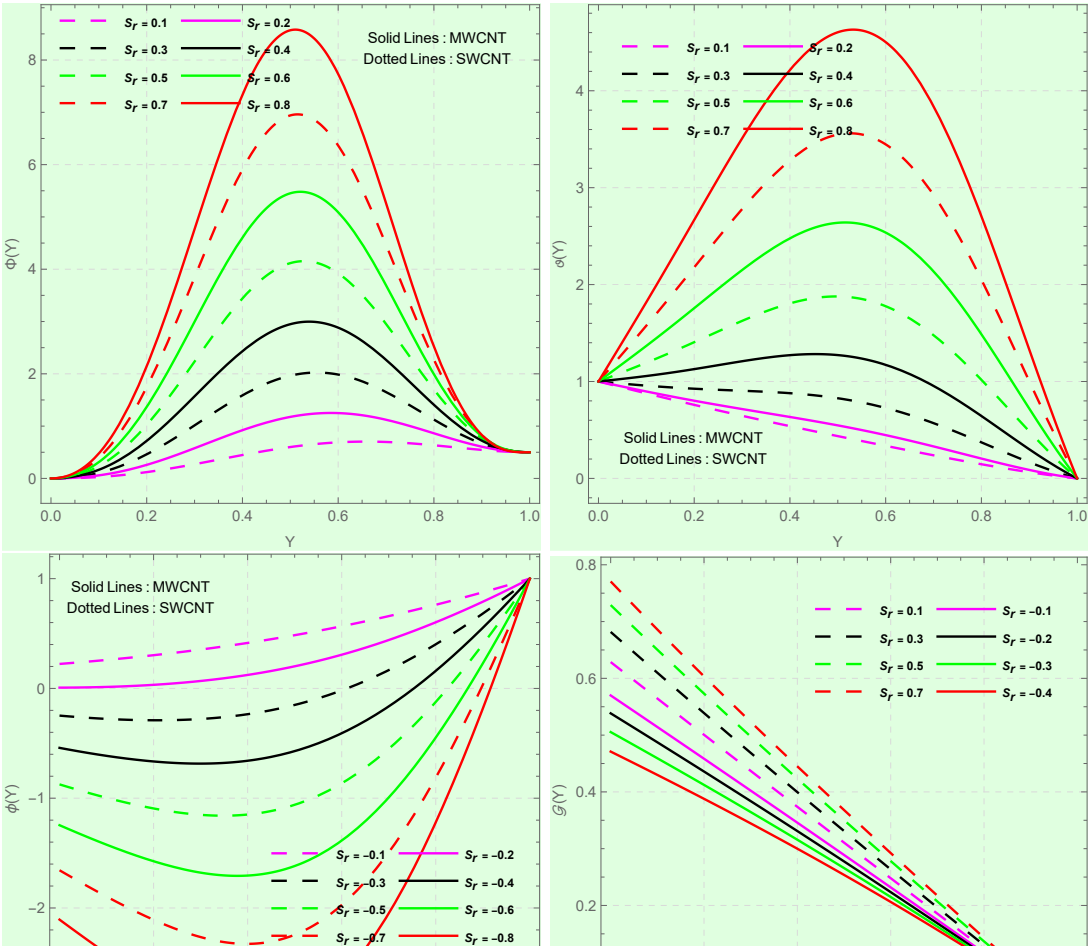

Plotting $\Phi(\Upsilon)$, $\vartheta(\Upsilon)$, $\varphi(\Upsilon)$, and (Υ) for both the single wall carbon nanotubes and multi wall carbon nanotubes cases in Figure 4 illustrates the impact of squeeze number S_r on the velocity and temperature distribution for both heating and cooling surfaces. The top plate is moving away from the lower stationary plate in this instance because the squeeze number values have been configured to be greater than zero, but the lower plate is moving away from the upper plate due to the reverse inequality of the squeeze number. A sketch of S_r's impact on $\Phi(\Upsilon)$ is presented for both the single wall carbon nanotubes and multi wall carbon nanotubes scenarios. Actually, when S_r increases, the top plate descends, applying more stress to the nanoparticles and raising the velocity components $\Phi(\Upsilon)$. A graph shows how S_r affects $\theta(\eta)$. For greater S_r, the top plate travels downward and the number of nanoparticle collisions rises, which raises the temperature and causes the concentration profiles of $\varphi(\Upsilon)$ to fall. The impact of the parameter S_r on the concentration profiles $\varphi(\Upsilon)$ and (Υ) is evident in Figure 4 for both single wall carbon nanotubes and multi wall carbon nanotubes. Due to a rise in S_r, it is noticed that the concentration profiles, $\varphi(\Upsilon)$ fall and (Υ) increases. The result indicates a decrease in viscosity due to an increase in the homogenous chemical process. On the other hand, Figure 4 shows that the $\varphi(\Upsilon)$ is the inverse of the (Υ).

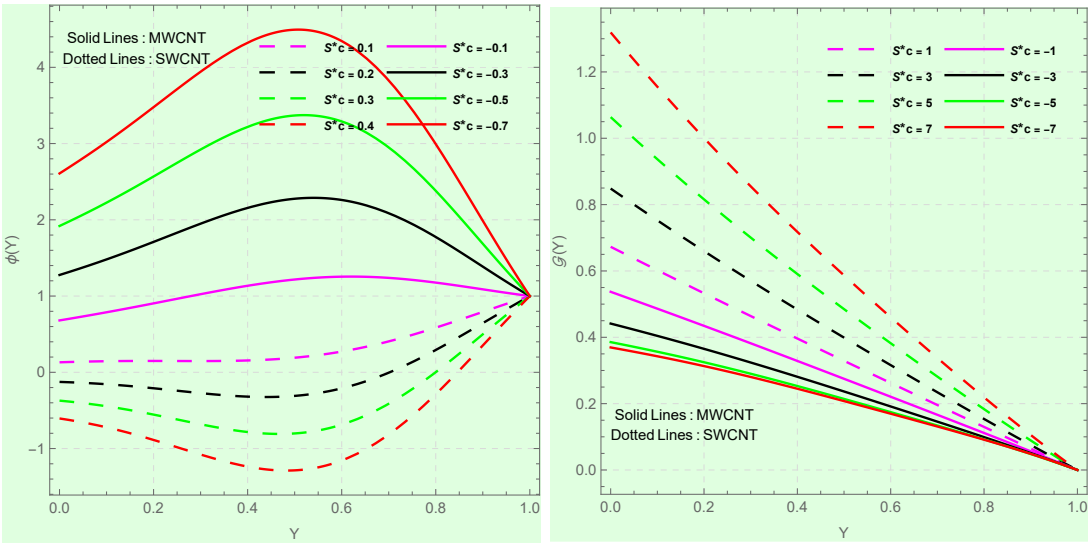

Figure 5: Impact of S_c^* on single wall carbon nanotubes and multi wall carbon nanotubes with $E_1 = 0.1$, $E_2 = 0.3$, $\phi_1 = 0.1$, $\phi_2 = 0.2$, $N = 1$, $M = 2$, $\beta = 1$, $P_r^* = 2$,$S_r = 2$, $h = 0.3$, $\delta = 0.1$, $\Gamma_1 = 1.1$, $\Gamma_2 = 1.5, \varphi a^* = 1$.

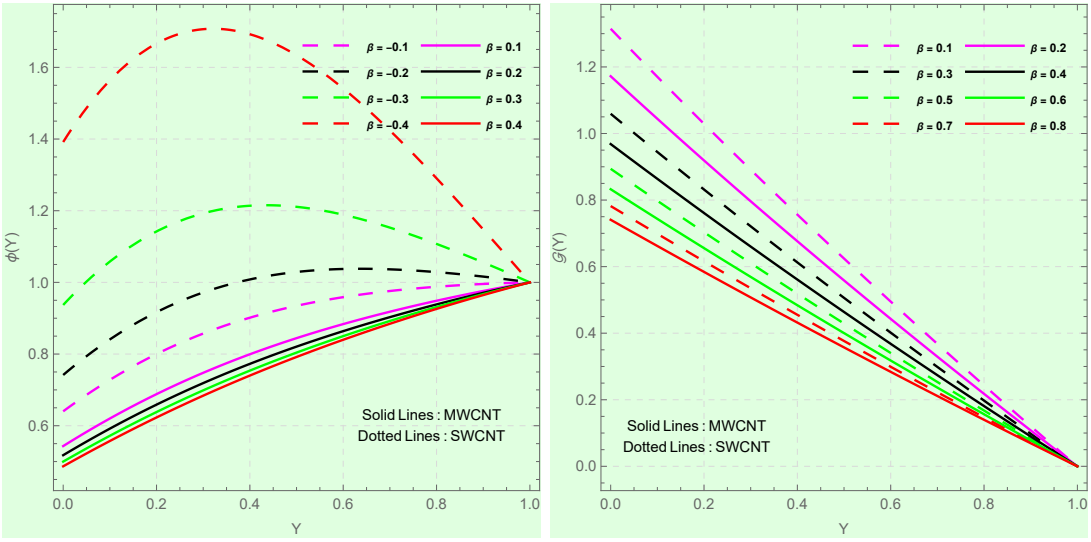

Figure 6: Impact of β on single wall carbon nanotubes and multi wall carbon nanotubes with $E_1 = 0.1$, $E_2 = 0.3$, $\phi_1 = 0.1$, $\phi_2 = 0.2$, $N = 1$, $M = 2$, $S^*c = 2$, $P_r^* = 2$,$S_r = 1$, $h = 0.3$, $\delta = 0.1$, $\Gamma_1 = 1.1$, $\Gamma_2 = 1.5, \varphi a^* = 1$.

Figure 5 demonstrates that for single wall carbon nanotubes and multi wall carbon nanotubes, the concentration boundary layer width decreases as the concentration profile $\varphi(\Upsilon)$ grows with increasing values of Schmidt's number S^*c. It is shown that when the diffusion coefficient of species falls, the reactant concentration increases more quickly; larger values of S^*c correspond to a quicker increase in the flow field concentration. Conversely, when the Schmidt number S^*c increases, the concentration profiles $\varphi(\Upsilon)$ and (Υ) drop.The effects of $\beta = \frac{D_A}{D_B} = 1$, the ratio of the diffusion coefficients, are displayed for both the single wall carbon nanotubes and multi wall carbon nanotubes cases on $\varphi(\Upsilon)$ and (Υ) in Figure 6. Figure 6 illustrates how the concentration profiles $\varphi(\Upsilon)$ and (Υ) grow with higher values of β. This diagram shows that $\varphi(\Upsilon)$ and (Υ) are reversed.

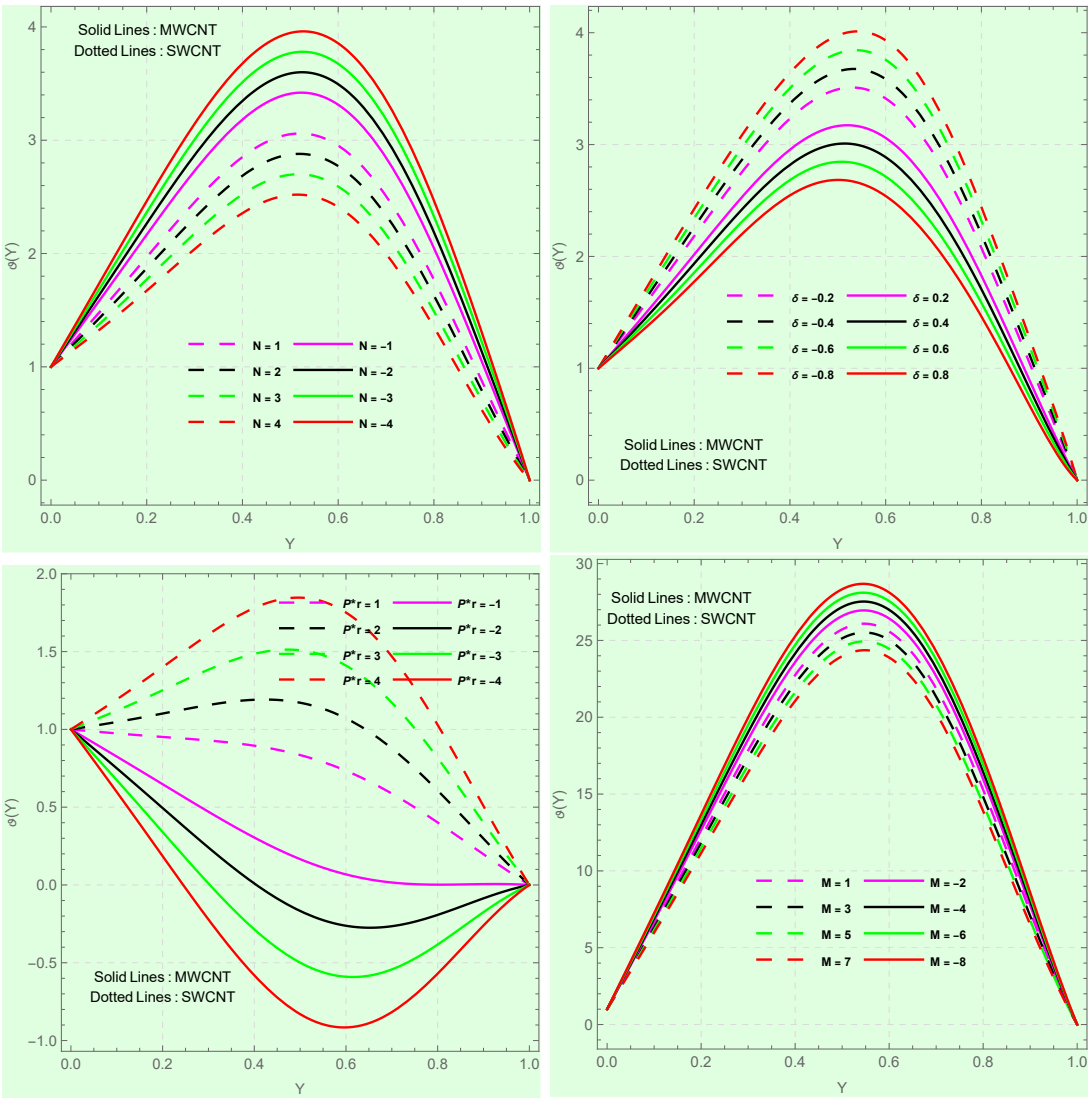

Figure 7: Impact of N, M, P_r^*, δ on single wall carbon nanotubes and multi wall carbon nanotubes with $E_1 = 0.1$, $E_2 = 0.3$, $\phi_1 = 0.1$, $\phi_2 = 0.2$, $S^*c = 2$, $S_r = 1$, $h = 0.3$, $\Gamma_1 = 1.1$, $\Gamma_2 = 1.5$, $\varphi a^* = 1$.

Figure 7 shows how the temperature profile is affected by the Prandtl number P_r^*, magnetic parameter, porosity parameter, and small parameter. The analysis reveals that in both single wall carbon nanotubes and multi wall carbon nanotubes cases, $\Phi(\Upsilon)$ and $\vartheta(\Upsilon)$ exhibit an inclining performance for high values of P_r^*. Since P_r^* is the ratio of momentum diffusivity to thermal diffusivity, greater values of P_r^* essentially increase the thickness of the boundary layer, which increases the cooling impact of the nanoparticle. Due to the closer packing of the nanoparticles in single wall carbon nanotubes compared to multi wall carbon nanotubes. Figure 7 shows that with a regular increase in the parameter M, the temperature distribution rises in the single wall carbon nanotubes and falls in the multi wall carbon nanotubes. In general, the increased values of M

in the multi wall carbon nanotubes lead to an enhancement of the fluid's temperature behaviour. Regular reductions in M will cause the fluid's thermal boundary layer thickness to decrease. The escorting hybrid ferrofluid physically generates the Lorentz force, which is a form of resistive force. In addition, the flow produces a certain quantity of thermal energy. For the porosity parameter N and tiny parameter δ, comparable outcomes are seen.

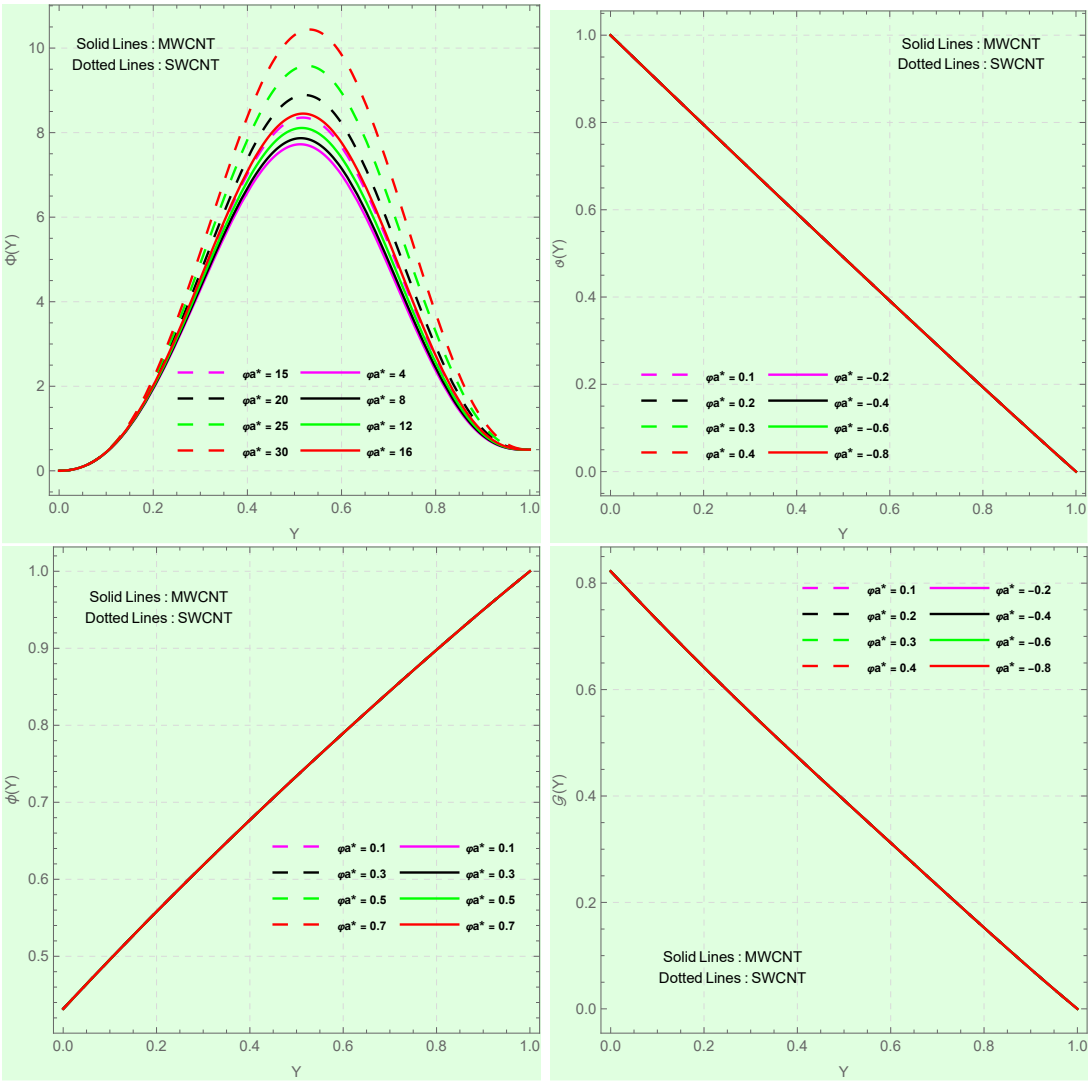

Figure 8: Impact of $\varphi a^* = 1$ on single wall carbon nanotubes and multi wall carbon nanotubes with $E_1 = 0.1$, $E_2 = 0.3$, $\phi_1 = 0.1$, $\phi_2 = 0.2$, $N = 1$, $M = 2$, $S^*c = 2$, $P_r^* = 2$,$S_r = 1$, $h = 0.3$, $\delta = 0.1$, $\Gamma_1 = 1.1$, $\Gamma_2 = 1.5$, $\beta = 1$.

For the phenomena of both the single wall carbon nanotubes and multi wall carbon nanotubes, Figure 8 illustrates the effect of the Hartmann number φa^* on $\Phi(\Upsilon)$, $\vartheta(\Upsilon)$, $\varphi(\Upsilon)$, and (Υ) against the similarity variable Υ.In single wall carbon nanotubes and multi

wall carbon nanotubes flow, the fluid velocity increases as we move along the horizontal axis, and the velocity is enhanced in the single wall carbon nanotubes and multi wall carbon nanotubes flows for the continuous positive change in the values of φa^*, while for the simultaneous cases, the same behaviour is shown in Figure 8. Furthermore, the liquid velocity is examined to ensure that the single wall carbon nanotubes and multi wall carbon nanotubes achieve maximum performance. In addition, $\vartheta(\Upsilon)$ exhibits the inverse behaviour. Figure 8 illustrates the influence of the Hartmann number on the thermal profile. Reduced thermal profile is the result of a rise in the Hartman number. Hartman number's effect on homogeneous and heterogeneous profiles is seen in Fig. 8, which displays results that are opposite to one another.

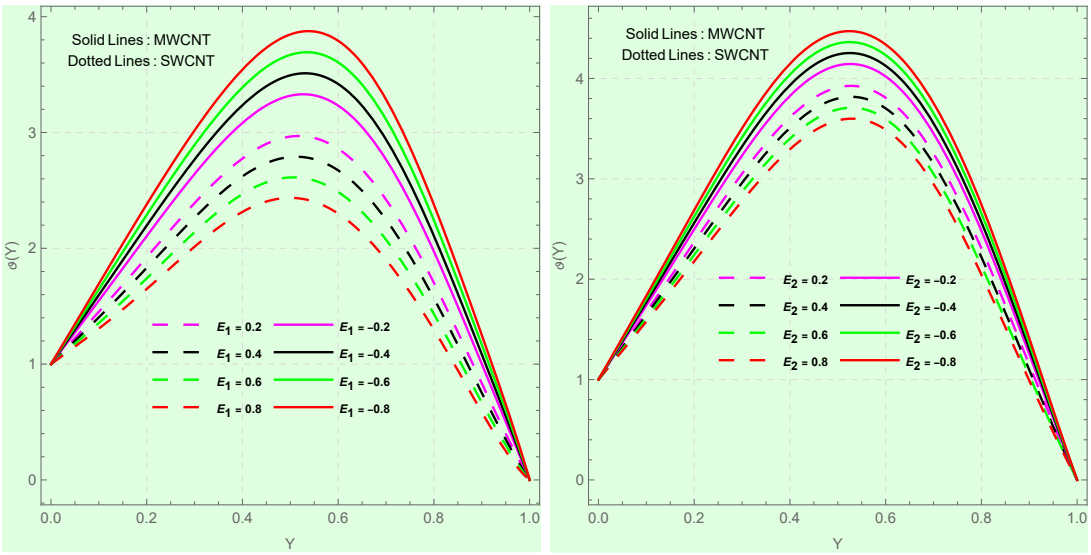

Figure 9: Impact of E_1, E_2 on single wall carbon nanotubes and multi wall carbon nanotubes with $\varphi a^* = 1$, $\phi_1 = 0.1$, $\phi_2 = 0.2$, $N = 1$, $M = 2$, $S^*c = 2$, $P_r^* = 2$,$S_r = 1$, $h = 0.3$, $\delta = 0.1$, $\Gamma_1 = 1.1$, $\Gamma_2 = 1.5$, $\beta = 1$.

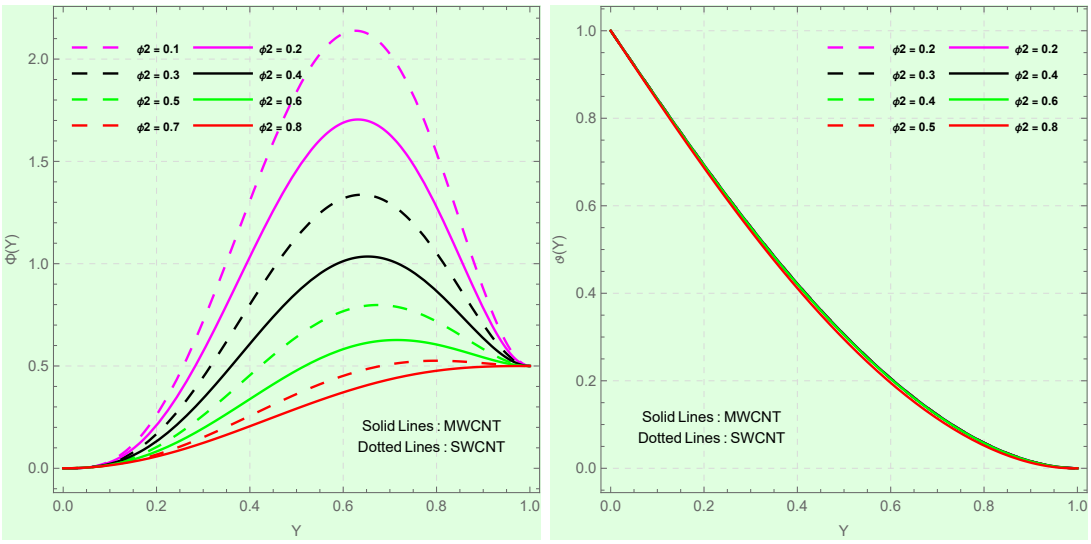

Figure 10: Impact of ϕ_2 on single wall carbon nanotubes and multi wall carbon nanotubes with $\varphi a^* = 1$, $E_1 = 1.1$, $E_2 = 1.5$, $\phi_1 = 0.1$, $\Gamma_1 = 1.1$, $\Gamma_2 = 1.5$, $N = 1$, $M = 2$, $S^*c = 2$, $P_r^* = 2$,$S_r = 1$, $h = 0.3$, $\delta = 0.1$, $\beta = 1$.

Figure 9 illustrates the concentration profile $\vartheta(\Upsilon)$ and the temperature-increasing behaviour in single wall carbon nanotubes and multi wall carbon nanotubes for higher local Eckert and Eckert numbers. Increasing the Eckert number, which measures frictional heat and viscous dissipation, leads to a rise in temperature. The thickness of the thermal boundary layer increases as the Eckert number increases, but the gradient of hybrid nanofluid temperature at the plate's surface, which is calculated using the local Nusselt number, decreases. This phenomenon may be explained by an increase in viscous dissipation, which raises the flow's thermal conductivity and strengthens the momentum and thermal boundary layers.

Figures (10–11) illustrate the effects of the volume fraction ϕ_1 and ϕ_2 of nanoparticles on the profiles of $\Phi(\Upsilon)$, $\vartheta(\Upsilon)$, $\varphi(\Upsilon)$, and (Υ) for (single wall carbon nanotubes) and (multi wall carbon nanotubes). However, it is clear that when the volume fraction parameters ϕ_1 and ϕ_2 are increased, the (single wall carbon nanotubes) and (multi wall carbon nanotubes) velocities are enhanced in the same manner. As a physical phenomenon, the rise in velocity is caused by the inverse relationship between the nanofluid's volume and dynamic viscosity. As a result, as the volume fraction increases, the normal fluid's viscosity falls, boosting fluid flow. Physically speaking, the higher volume fraction produces more energy transferred through the fluid flow associated with the uneven development of the ultra-fine materials, which leads to a notable increase in the friction factor and the rate of heat transfer. In both flows, the heat transfer rate and the friction factor are increased by the squeezed parameter. For volume concentration parameters, the inverse pattern is seen in both the homogeneous and heterogeneous profiles.

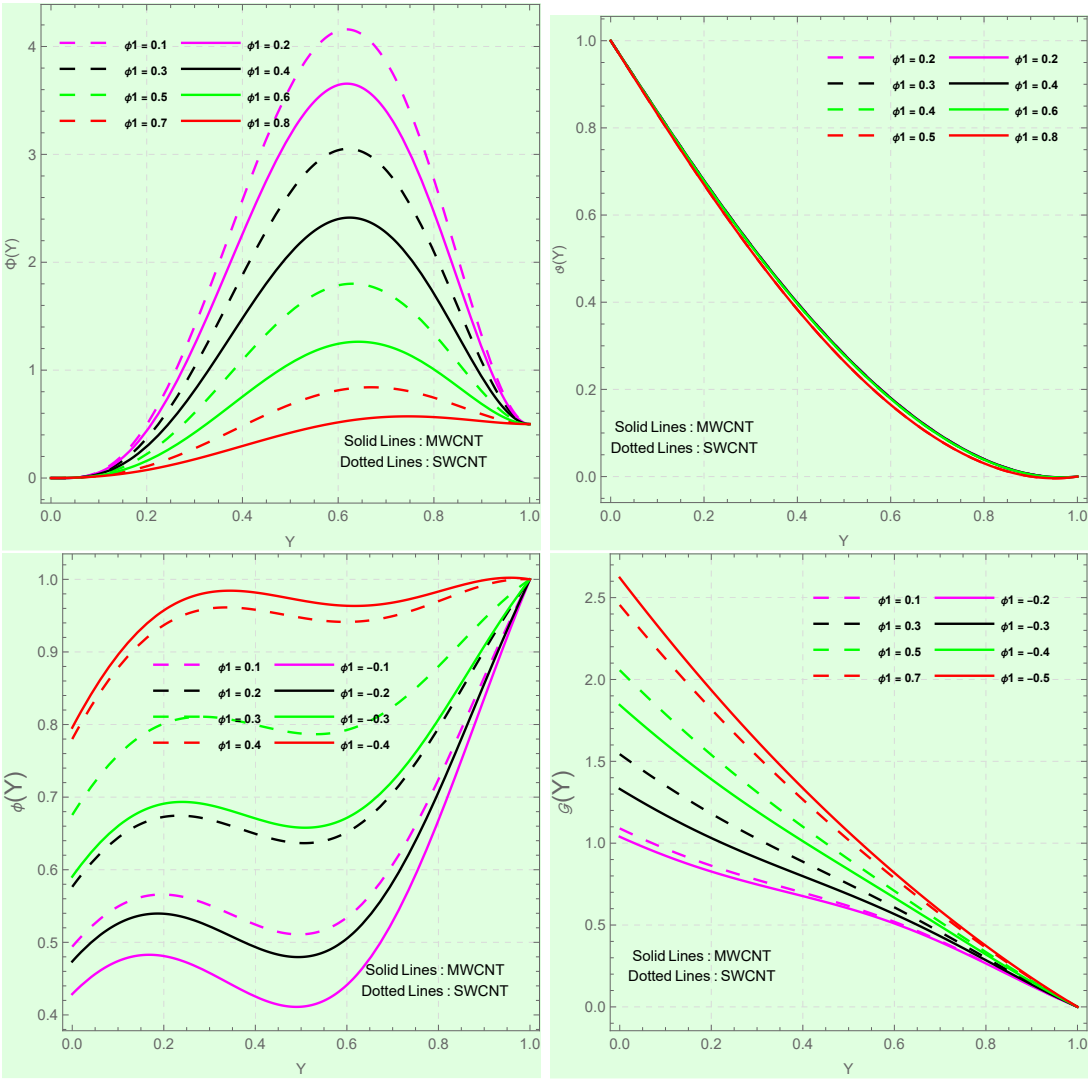

Figure 11: Impact of ϕ_1 on single wall carbon nanotubes and multi wall carbon nanotubes with $\varphi a^* = 1$, $E_1 = 1.1$, $E_2 = 1.5$, $\phi_2 = 0.2$, $\Gamma_1 = 1.1$, $\Gamma_2 = 1.5$, $N = 1$, $M = 2$, $S^*c = 2$, $P_r^* = 2$,$S_r = 1$, $h = 0.3$, $\delta = 0.1$, $\beta = 1$.

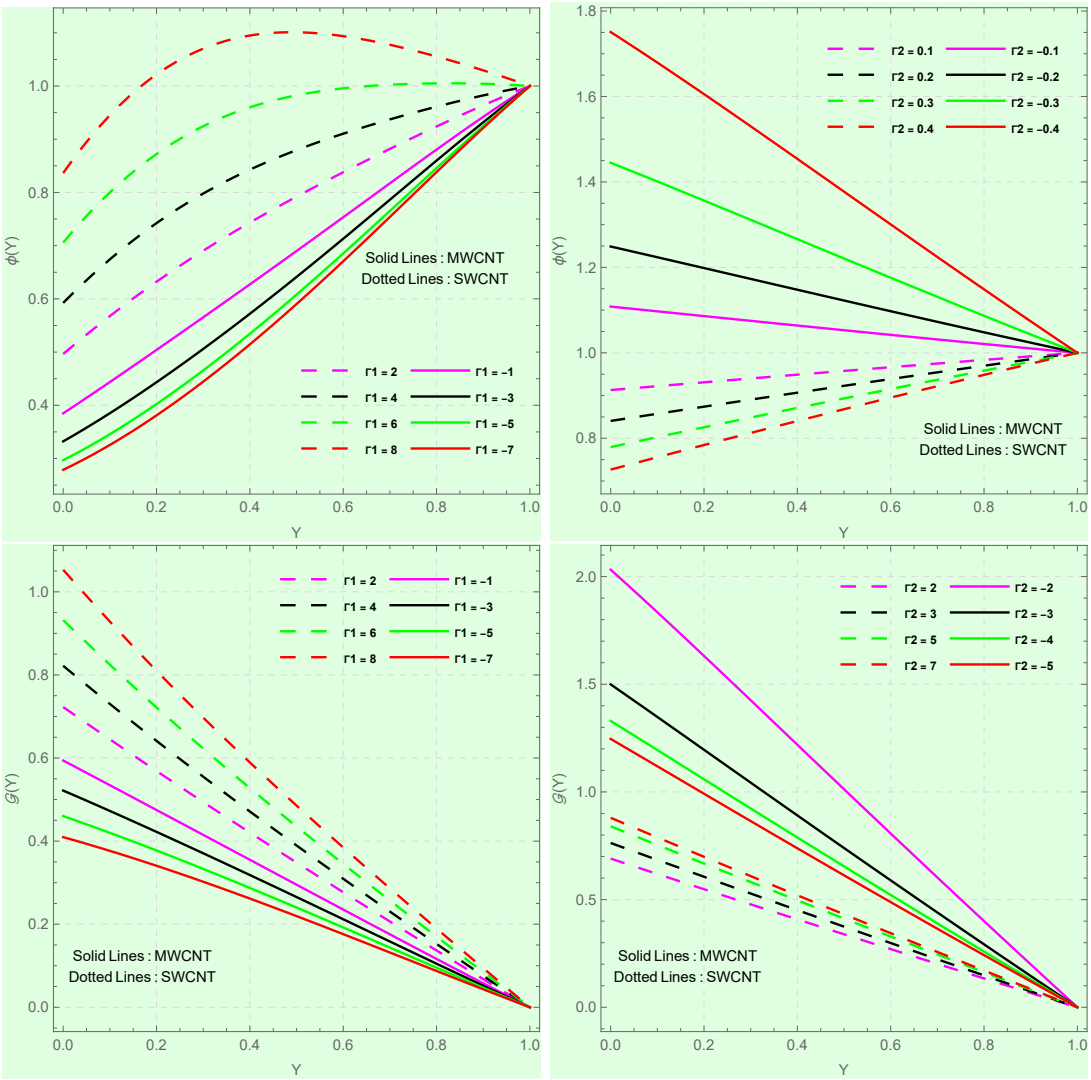

Figure 12: Impact of Γ_1, Γ_2 on single wall carbon nanotubes and multi wall carbon nanotubes with $\varphi a^* = 1$, $E_1 = 1.1$, $E_2 = 1.5$, $\phi_1 = 0.1$, $\phi_2 = 0.2$, $N = 1$, $M = 2$, $S^*c = 2$, $P_r^* = 2$,$S_r = 1$, $h = 0.3$, $\delta = 0.1$, $\beta = 1$.

Figure 12 shows the effects of the equations describing the homogeneous strength parameter Γ_1 and the heterogeneous strength parameter Γ_2 on the concentration profiles $\varphi(\Upsilon)$ and (Υ). An increase in $\varphi(\Upsilon)$ and (Υ) concentration profiles. It is shown that when Γ_1 increases, the homogeneous chemical reaction parameter also increases, and viscosity reduces as a result. At decreasing strengths of the homogeneous reaction parameter, the concentration profile rises while the thickness of the border layer falls. It is observed that the concentration distribution decreases as the heterogeneous reaction intensity Γ_2 increases. Increased concentration fields are caused by highly dispersed particles, which are strongly correlated with higher values of Γ_2. Nevertheless, Figure 12 illustrates how the impact on concentration profiles, $\varphi(\Upsilon)$, shows that a homogeneous strength parameter,

Γ_1, and a heterogeneous strength parameter, Γ_2, are opposite of one another.

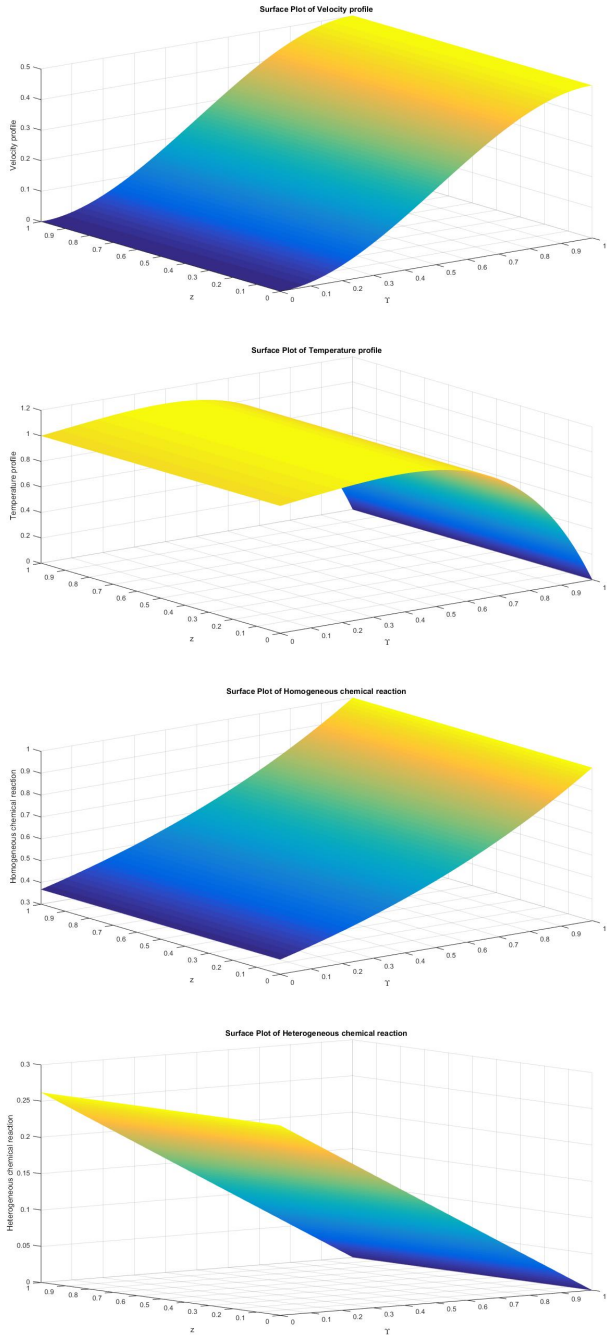

Figure 13: Impact on $\Phi(\Upsilon)$, $\vartheta(\Upsilon)$, $\varphi(\Upsilon)$ and (Υ) for multi wall carbon nanotubes with $S_r = -0.2$, $P_r^* = 0.1$, $\delta = 0.1$, $\delta = 0.1$, $E_1 = 0.1$, $E_2 = 0.2$, $S^*c = 0.1$, $\Gamma_1 = 0.5$ $\Gamma 2 = -1.3$, $N = 0.1$, M=0.5, $\beta = 0.7$, $\phi 1 = 0.1$, $\phi 2 = 0.2$, $\varphi a^* = 0.1$.

Figure 13 illustrates the effect of the similarity variable Υ on $\Phi(\Upsilon)$, $\vartheta(\Upsilon)$, $\varphi(\Upsilon)$, and (Υ) for the carbon nanotubes phenomenon in the case of three dimensions

7. Conclusion

This work examines heat transmission, two-dimensional fluid flow between two squeezing plates, Joule heating, viscous dissipation, and homogeneous and heterogeneous chemical reactions in the presence of carbon nanotubes nanoparticles. There hasn't been a study that looks at the combined effects of carbon nanotube nanoparticles on unstable flow between two squeezing plates. Subsequently, we used all the data to look at how a uniform and heterogeneous chemical reaction affected the flow between two compressing plates with carbon nanotube nanoparticles attached. New insights into the interplay of homogeneous-heterogeneous chemical processes, viscous dissipation, and Joule heating on mass and heat transfer behaviour are provided by their combined inclusion.Squeeze flow, which has not been thoroughly investigated in previous research, will be systematically investigated utilising hybrid nanofluids (carbon nanotubes + alumina nanoparticles). After transforming PDEs into ODEs, BVP4c and Homotopy analysis method solved the simplified governing equation. Graphs have been used to show how different factors affect the concentration, temperature, and velocity profiles, as well as the skin friction coefficient and local Nusselt number change caused by the impacts of interest parameters. The analysis reveals several important trends in the flow and heat transfer characteristics of carbon nanotubes-based nanofluids under squeezing conditions. The parameters S_r, ϕ_1, ϕ_2, and φa^* are found to enhance the fluid velocity, whereas S_c, β, Γ_1, and Γ_2 act to suppress it. Similarly, the fluid temperature rises with increasing $P_r^*, \delta, \varphi a^*, \phi_1$, and ϕ_2, but decreases with N, M, E_1, and E_2. The incorporation of carbon nanotubess leads to a reduction in volume fraction and an increase in the squeezed Reynolds number, which subsequently enhances skin friction. Moreover, the local Nusselt number decreases with decreasing squeeze numbers and increasing Prandtl numbers, volume fractions, and Eckert numbers. A thicker carbon nanotubes nanofluid layer intensifies the cooling effect and simultaneously increases both skin friction and the Nusselt number by enhancing the resistance force driving the flow motion, with single wall carbon nanotubess exhibiting a stronger influence compared to multi wall carbon nanotubess. The Eckert number further influences the thermal field by raising the nanofluid temperature through viscous dissipation effects, more prominently in the case of single wall carbon nanotubess. Overall, both types of carbon nanotubes significantly affect skin friction and the Nusselt number, as confirmed by the numerical results. The semi-analytical Homotopy analysis method solutions and the numerical bvp4c results exhibit excellent agreement, indicating the high accuracy and reliability of the adopted methodologies.

8. Limitations and Future Work

This section explicitly acknowledges the simplifying assumptions adopted in the present model, as well as the potential sources of error and avenues for future improvement. The

added discussion emphasises the following points:
Modeling Assumptions: The analysis assumes idealised homogeneous–heterogeneous reaction mechanisms, simplified nanoparticle–fluid interactions, and the use of a slip boundary condition model. These assumptions neglect possible agglomeration, Brownian motion, and non-Newtonian effects that may occur in real nanofluid systems.
Thermal and Flow Conditions: The boundary conditions are treated as uniform and steady, whereas in practical applications variations in wall temperature, surface roughness, or unsteady squeezing may alter the system response.
Numerical Method Constraints: Although Homotopy analysis method and bvp4c both produce accurate and consistent results, Homotopy analysis method is dependent on the choice of convergence-control parameters, while bvp4c may require fine meshing for highly stiff systems. These factors could limit efficiency for more complex geometries.
Applicability Range: The present model is developed for parallel-plate squeeze flow and may not directly extend to three-dimensional or turbulent configurations. Its predictions are most applicable within laminar, microscale, and lubrication-type systems.

References

[1] S. Iijima. Helical microtubules of graphitic carbon. *Nature*, 354:56–58, 1991.
[2] A. Oberlin, M. Endo, and T. Koyama. Filamentous growth of carbon through benzene decomposition. *Journal of Crystal Growth*, 32:335–349, 1976.
[3] S. Iijima and T. Ichihashi. Single-shell carbon nanotubes of 1-nm diameter. *Nature*, 363:603–605, 1993.
[4] D. S. Bethune, C. H. Kiang, M. S. Devries, G. Gorman, R. Savoy, J. Vazquez, et al. Cobalt-catalysed growth of carbon nanotubes with single-atomic-layer walls. *Nature*, 363:605–607, 1993.
[5] M. Terrones. Science and technology of the twenty-first century: synthesis, properties, and applications of carbon nanotubes. *Annual Review of Materials Research*, 33:419–501, 2003.
[6] M. F. L. De Volder, S. H. Tawfick, R. H. Baughman, and A. J. Hart. Carbon nanotubes: present and future commercial applications. *Science*, 339:535–539, 2013.
[7] F. Mebarek-Oudina, M. Bouselsal, S. U. Khan, K. Ramesh, and A. I. Ismail. Optimizing thermal performance in shell-and-tube heat exchangers with tri-hybridised nanofluids: a numerical study of turbulent convection. *Thermal Science and Engineering Progress*, page 103988, 2025.
[8] T. Naseem, F. Mebarek-Oudina, H. Vaidya, N. Bibi, K. Ramesh, and S. U. Khan. Numerical analysis of entropy generation in joule heated radiative viscous fluid flow over a permeable radially stretching disk. *Computational Modeling in Engineering and Sciences*, 143(1):1, 2025.
[9] F. Mebarek-Oudina, M. Bouselsal, R. Djebali, H. Vaidya, N. Biswas, and K. Ramesh. Thermal performance of mgo-swcnt/water hybrid nanofluids in a zigzag walled cavity with differently shaped obstacles. *Modern Physics Letters B*, page 2550163, 2025.
[10] L. Qiu, X. Wang, D. Tang, X. Zheng, P. M. Norris, D. Wen, J. Zhao, X. Zhang, and

Q. Li. Functionalization and densification of inter-bundle interfaces for improvement in electrical and thermal transport of carbon nanotube fibers. *Carbon*, 105:248–259, 2016.

[11] L. Qiu, N. Zhu, H. Zou, Y. Feng, X. Zhang, and D. Tang. Advances in thermal transport properties at nanoscale in china. *International Journal of Heat and Mass Transfer*, 125:413–433, 2018.

[12] Z. Zaidi, S. T. Mohyud-din, and B. B. Mohsen. Convective heat transfer and mhd analysis of wall jet flow of nanofluids containing carbon nanotubes. *Engineering Computations*, 34:1–9, 2017.

[13] P. Sreedevi, P. S. Reddy, and A. J. Chamkha. Magneto-hydrodynamics heat and mass transfer analysis of single and multi - wall carbon nanotubes over vertical cone with convective boundary condition. *International Journal of Mechanical Science*, 135:646–655, 2018.

[14] R. U. Haq, F. Shahzad, and Qasem M. Al-Mdallal. Mhd pulsatile flow of engine oil based carbon nanotubes between two concentric cylinders. *Results in Physics*, 7:57–68, 2017.

[15] Q. Xue. Model for thermal conductivity of carbon nanotube-based composites. *Physica B: Condensed Matter*, 368:302–307, 2005.

[16] I. D. Garbadeen, M. Sharifpur, J. M. Slabber, and J. P. Meyer. Experimental study on natural convection of mwcntwater nanofluids in a square enclosure. *International Communications in Heat and Mass Transfer*, 88:1–8, 2017.

[17] U. Khan, N. Ahmed, S. T. Mohyud-Din, and W. Sikander. Flow of carbon nanotubes suspended nanofluid in stretchable non-parallel walls. *Neural Computing and Applications*, 2017. DOI: 10.1007/s00521-017-2891-1.

[18] S. K. Sahoo. A comprehensive review of multi-criteria decision-making (mcdm). *Spectrum of Operational Research*, 2(1):268–284, 2025.

[19] M. Farooq, A. U. Rahman, A. Khan, I. Ozsahin, B. Uzun, and H. Ahmad. Comparative analysis of magnetohydrodynamic inclined poiseuille flow of couple stress fluids. *Journal of Computational Applied Mechanics*, 56(3):536–560, 2025.

[20] S. A. Ali and T. Gul. The convective study of the al2o3-h2o and cu-h2o nano-liquid film sprayed over a stretching cylinder with viscous dissipation. *The European Physical Journal Plus*, 132:495, 2017.

[21] E. Simsek. Evaluation of purchasing process in solar energy investment projects via siwec methodology. *Spectrum of Operational Research*, 3(1):81–86, 2025.

[22] M. Farooq, R. Nawaz, A. Khan, F. Shahid, I. Ozsahin, B. Uzun, and H. Ahmad. Comparative study of non-isothermal poiseuille flow of couple stress fluid in reynolds model between inclined plates using two homotopy-based methods. *Journal of Computational Applied Mechanics*, 56(3):587–601, 2025.

[23] A. U. Rehman, R. Mehmood, S. Nadeem, N. S. Akbar, and S. S. Motsa. Effects of single and multi-walled carbon nano tubes on water and engine oil based rotating fluids with internal heating. *Advanced Powder Technology*, 28(9):1991–2002, 2017.

[24] R. Ellahi, M. Hassan, and A. Zeeshan. Study of natural convection mhd nanofluid by means of single and multiwalled carbon nanotubes suspended in a salt water solution.

IEEE Transactions on Nanotechnology, 14(4):1–10, 2015.

[25] M. Sajid, T. Hayat, and S. Asghar. Non-similar solution for the axisymmetric flow of a third-grade fluid over a radially stretching sheet. *Acta Mechanica*, 189:193–205, 2007.

[26] T. Gul. Scattering of a thin layer over a nonlinear radially extending surface with magneto hydrodynamic and thermal dissipation. *Surface Review and Letters*, 1850123:1–7, 2018. DOI: 10.1142/S0218625X18501238.

[27] J. V. Ramana Reddy, V. Sugunamma, and N. Sandeep. Effect of frictional heating on radiative ferrofluid flow over a slendering stretching sheet with aligned magnetic field. *The European Physical Journal Plus*, 132:article, 2017.

[28] J. V. Ramana Reddy, V. Sugunamma, and N. Sandeep. Effect of nonlinear thermal radiation on mhd flow between rotating plates with homogeneous-heterogeneous reactions. *International Journal of Engineering Research in Africa*, 20:130–143, 2015.

[29] R. Jawad, M. R. Azizah, and O. Zurni. Numerical investigation of copper-water (cu-water) nanofluid with different shapes of nanoparticles in a channel with stretching wall: slip effects. *Mathematical and Computational Applications*, 21:43–58, 2016.

[30] J. H. Merkin. A model for isothermal homogeneous-heterogeneous reactions in boundary-layer flow. *Mathematical and Computer Modelling*, 24(8):125–136, 1996.

[31] J. H. Merkin. A model for isothermal homogeneous and heterogeneous reactions in boundary layer flow. *Mathematical and Computer Modelling*, 24(8):125–136, 1996.

[32] M. Sheikholeslami, M. M. Rashidi, D. M. Al Saad, F. Firouzi, H. B. Rokini, and G. Domairrry. Steady nanofluid flow between parallel plates considering thermophoresis and brownian effects. *Journal of King Saud University - Science*, 2015. http://dx.doi.org/10.1016/j.jksus.,06.003.

Nomenclatures

μ	Dynamic viscosity
P	Pressure of fluid
$(\rho)_{CNT}$	Effective density
$(\rho c_p)_{CNT}$	Specific heat capacity
$(\sigma)_{CNT}$	Electrical conductivity
$(\kappa)_{CNT}$	Thermal conductivity
ψ, ν	Velocity components
φ	Temperature distribution

φ_u, φ_l	Upper and lower plates temperatures
D_Ω, D_B^*	Diffusion coefficients of the chemical species
β	Ratio of the diffusion coefficients
Γ_1	Homogeneous reaction strength
Γ_2	Heterogeneous reaction strength
S_r	Squeeze Reynolds number
P_r^*	Prandtl number
$\varphi^* a$	Hartman number
C_f	Skin-friction coefficient
Nu	Local Nusselt number
Sh	Sherwood number
$\Omega 1$, $\Omega 2$	Chemical species
E_1	Local Eckert number
E_2	Eckert numbers
N	Porosity parameter
δ	Small parameter
S_c^*	Schmidt number
M	Magnetic field parameter
ϕ_1, ϕ_2	The volume fraction of the individual particles
hnf	Hybrid nanofluid
snf	Single nanofluid